International Journal of Heat and Mass Transfer 186 (2022) 122497

Contents lists available at ScienceDirect

International Journal of Heat and Mass Transfer

journal homepage: www.elsevier.com/locate/hmt

Performance characteristics of a divergent vortex tube

James Cartlidge, Nafiz Chowdhury, Thomas Povey*

Department of Engineering Science, University of Oxford, Parks Road, Oxford OX1 3PJ, UK

ARTICLE INFO

Article history:
Received 7 July 2021
Revised 21 December 2021
Accepted 27 December 2021
Available online 18 January 2022

Keywords:
Ranque-Hilsch
Vortex tube
Refrigerator
Refrigeration
Energy separation
Coefficient of performance
Turbomachinery

ABSTRACT

In this paper performance characteristics for a Ranque-Hilsch vortex tube are presented. The vortex tube was of divergent design and optimised for both size and performance, to be used to supply cold air to turbomachinery experiments with feed air in the supply pressure range 3.0–7.0 bar, and with overall feed mass flow rates in the range 0.05–0.14 kg/s. Optimum fixed parameters selected from the literature were: the ratio of cold-exit diameter to tube inlet internal diameter (0.50); the ratio of combined inlet-nozzle throat area to the tube inlet internal cross-sectional area (0.22); the vortex tube half-angle (3°); the number of inlet nozzles (6); the half-angle of the hot exhaust conical splitter (45°) and the ratio of tube length to tube inlet internal diameter (20). Free parameters that were investigated were: the overall total-to-static pressure ratio between inlet and cold-exit conditions (3.0, 5.0, and 7.0) and the cold-gas mass fraction (0.0–1.0). Comprehensive experiments were performed to characterise the vortex tube performance in terms of the following parameters: non-dimensional cold and hot-outlet temperatures; non-dimensional cold and hot-gas energy separation; isentropic efficiency referenced to cold-gas expansion; and coefficient of performance (COP). A transient heat flux correction technique was implemented to correct for unsteady heat flux terms from the working gas to the vortex chamber walls. Joule-Thomson effects were accounted for by introducing a corrected inlet total temperature. Cold-exit and hot-exit temperature separations were found to increase with pressure ratio. Non-dimensional cold-exit temperature had a minimum at cold-gas mass fraction of approximately 0.40. Non-dimensional hot-exit temperature increased approximately linearly with cold-gas mass fraction. COP decreased with increasing pressure ratio and had a peak value at cold-gas mass fraction approximately 0.60. Isentropic efficiency was relatively insensitive to pressure ratio and had a peak value at cold-gas mass fraction approximately 0.23. In the range investigated the lowest non-dimensional cold-exit temperature (normalised by inlet temperature) was 0.91, the highest coefficient of performance was 0.097, and the highest isentropic efficiency was 0.23. Full details of the design are given, allowing implementation by other researchers.

1. Introduction

The vortex tube is a thermodynamic device that separates an incoming stream of fluid into hot and cold exit streams. This phenomenon is known as energy separation and—in the vortex tube—is achieved through viscous work and heat transfer, without the need for moving parts. The principle was originally developed by Ranque [1] in the 1930s. Many researchers have since optimised the design.

The most widely used vortex tube design is the counter-flow Ranque-Hilsch vortex tube (RHVT). A schematic representation is given in Fig. 1, showing a RHVT with a divergent tube section, as used in the current study. Compressed air enters the vortex chamber at high speed and with a high whirl angle through the inlet nozzles. Two structures develop, an external vortex which has net flow towards the hot exit, and an internal vortex which has net flow towards the cold exit. The ball valve downstream of the hot exit (shown in Fig. 2) controls the hot-gas mass flow, and, simultaneously, the vortex tube operating pressure. For a given design this sets the cold-gas mass fraction, ε, defined by

$$\varepsilon = \frac{\dot{m}_c}{\dot{m}_1} \tag{1}$$

where $\dot{m}_c$ is the cold-exit mass flow rate and $\dot{m}_1$ is the inlet mass flow rate. In the vortex tube studied in this paper, the pressure downstream of the cold exit was approximately atmospheric. The overall total-to-static pressure ratio between inlet and cold-exit conditions, p_{01}/p_c, was set by adjusting the system inlet pressure.

Although there are a number of studies of vortex tube performance in the open literature, few of these present comprehensive

* Corresponding author.
E-mail address: thomas.povey@eng.ox.ac.uk (T. Povey).

https://doi.org/10.1016/j.ijheatmasstransfer.2021.122497

Nomenclature

A	vortex tube inlet internal cross-sectional area, m^2
A_1	combined inlet nozzle throat area, m^2
A_a	inner wall surface area, m^2
A_b	outer wall surface area, m^2
c_p	specific heat capacity at constant pressure, J/(kg K)
c_v	specific heat capacity at constant volume, J/(kg K)
C	constant used in Nusselt number correlation, –
C_d	discharge coefficient, –
d_c	cold-exit orifice plate diameter, m
D	vortex tube internal diameter at inlet, m
D_e	vortex tube internal diameter at exit, m
D_b	vortex tube outer diameter, m
dt	time increment, s
E_c	cold-gas energy separation parameter, –
E'_c	cold-gas energy separation parameter, corrected for transient heat flux, –
E_h	hot-gas energy separation parameter, –
E'_h	hot-gas energy separation parameter, corrected for transient heat flux, –
h	convective heat transfer coefficient, W/(m^2 K)
k_1	constant used in transient correction, –
k	thermal conductivity, W/(m K)
L	tube length, m
m	exponent used in Nusselt number correlation, –
$\dot{m}_1$	inlet mass flow rate, kg/s
$\dot{m}_c$	cold-exit mass flow rate, kg/s
$\dot{m}_h$	hot-exit mass flow rate, kg/s
M	mass of vortex tube section, kg
N	number of inlet nozzles, –
p	static pressure, Pa
p_0	total pressure, Pa
p_{01}	inlet total pressure, Pa
p_{atm}	atmospheric pressure, Pa
p_c	cold-exit static pressure, Pa
p_h	hot-exit static pressure, Pa
$\dot{Q}$	heat flux from cold-exit to hot-exit stream, W
$\dot{Q}_A$	heat flux out of the fluid control volume, W
$\dot{Q}_B$	free convection heat flux between outer wall and environment, W
$\dot{Q}_C$	net heat flux absorbed by the tube walls, W
$\dot{Q}_R$	residual heat flux, W
r	outer radius of hot-exit conical splitter, m
s	specific entropy, J/(kg K)
t	time, s
T_0	total temperature, K
T_{01}	inlet total temperature, K
T^*_{01}	Joule-Thomson corrected inlet total temperature, K
T_{0c}	cold-exit total temperature, K
T'_{0c}	cold-exit total temperature, corrected for transient heat flux, K
T_{0h}	hot-exit total temperature, K
T'_{0h}	hot-exit total temperature, corrected for transient heat flux, K
T_w	average of internal and external wall temperatures, K
T_{wa}	internal wall temperature, K
T_{wb}	external wall temperature, K
$\dot{W}$	work rate due to viscous shear stress, W

Greek symbols

α	minimization parameter, –
β	vortex tube divergence half-angle, degrees
γ	ratio of specific heat capacities, –
Δ	change in quantity, –
ε	cold-gas mass fraction, –
η_1	isentropic efficiency referenced to cold gas expansion, –
η'_1	isentropic efficiency referenced to cold gas expansion, corrected for transient heat flux, –
η_2	isentropic efficiency referenced to inlet stream expansion, –
η'_2	isentropic efficiency referenced to inlet stream expansion, corrected for transient heat flux –
θ_c	non-dimensional cold-exit total temperature, –
θ_h	non-dimensional hot-exit total temperature, –
θ'_c	non-dimensional cold-exit total temperature, corrected for transient heat flux, –
θ'_h	non-dimensional hot-exit total temperature, corrected for transient heat flux, –
θ^*_c	non-dimensional cold-exit total temperature, corrected for Joule-Thomson effect, –
θ^*_h	non-dimensional hot-exit total temperature, corrected for Joule-Thomson effect, –
λ_c	cold-exit temperature separation normalised by its settled value, –
λ_h	hot-exit temperature separation normalised by its settled value, –
λ_R	root-mean-square of λ_c and λ_h, –
λ'_c	cold-exit temperature separation, corrected for transient heat flux, normalised by its settled value, –
λ'_h	hot-exit temperature separation, corrected for transient heat flux, normalised by its settled value, –
λ'_R	root-mean-square of λ'_c and λ'_h, –
τ	time constant of each vortex tube zone, s
φ	hot-exit conical splitter half-angle, degrees

Subscript

0	stagnation conditions
1 to 6	station numbers
a	inner wall
amb	ambient conditions
b	outer wall
c	cold-exit conditions
f	mean film properties
h	hot-exit conditions
j	station number
nt	nozzle throat conditions
up	conditions upstream of venturi nozzle

Abbreviations

COP_c	coefficient of performance as refrigerator
COP'_c	coefficient of performance as refrigerator, corrected for transient heat flux
Gr	Grashof number
Nu	Nusselt number
Pr	Prandtl number

performance parameters over a wide range of operating conditions. The aim of the current study is to close this literature gap by providing comprehensive performance curves for a vortex tube with design parameters optimised according to current literature.

1.1. Vortex tube design (fixed parameters)

The fixed parameters in the current study are now described, and chosen values are justified with reference to design optimums in the literature.

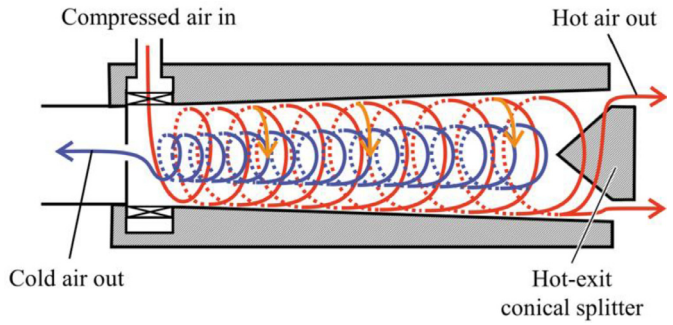

Fig. 1. Schematic representation of RHVT.

Early experimental work by Raiskii and Tunkel [2] investigated the effect on votex tube performance of the ratio of tube length to inlet internal diameter (in the range $2.0 < L/D < 40.0$) and shape (cylindrical and conical-diffuser). Experiments were conducted in the range $0.10 < \varepsilon < 1.00$ and $3.0 < p_{01}/p_c < 5.0$. Results showed that diffusers provide less cold-exit temperature separation than straight tubes of equivalent length and that cold-exit temperature separation rises with increasing length, but asymptotically so for high L/D.

More recently, Aydin and Baki [3] performed an extensive experimental study of the performance of cylindrical vortex tubes. Fixed parameters were: $d_c/D = 0.28$; and $N = 1$. Free parameters were: $0.00 < \varepsilon < 1.00$; $3.0 < p_{01}/p_c < 5.0$; $0.08 < A_1/A < 0.15$; $14 < L/D < 42$; hot-exit conical splitter half-angle, $25^\circ < \varphi < 30^\circ$; and working fluid (nitrogen, oxygen and air). They found the following: cold-exit and hot-exit temperature separation decreased as φ increased; highest cold-exit temperature separation was achieved for a ratio of inlet-nozzle throat area to tube internal cross-sectional equal to $A_1/A = 0.11$; cold-exit temperature separation increased as L/D increased in the range $0 < L/D \leq 20$ and decreased in the range $20 < L/D \leq 42$; the combination $\varphi = 25^\circ$, $L/D = 20$ and $d_c/D = 0.34$ at $p_{01}/p_c = 5.0$ and $\varepsilon = 0.20$ gave the highest cold-exit temperature separation for any condition tested. They show that nitrogen gave the highest temperature separation of the three working fluids tested (not fully explained). In the current study $L/D = 20$ was chosen as a fixed parameter.

The shape of the hot exhaust valve has been shown to affect vortex tube performance. Pise and Devade [4] experimentally studied the effects of hot-exit conical splitter half-angle, φ, on vortex tube performance for a cylindrical vortex tube with conical-step diffuser. Free parameters were $15^\circ < \varphi < 45^\circ$ and $2.0 < p_{01}/p_c < 6.0$. They found maximum cold-exit and hot-exit temperature separation occurred for $p_{01}/p_c = 6.0$ with $\varphi = 22.5^\circ$ and $\varphi = 45^\circ$, respectively. In the current study $\varphi = 45^\circ$ was chosen as a fixed parameter.

The ratio of cold-exit orifice diameter to vortex tube internal diameter has also been shown to affect performance. In experiments with cylindrical vortex tubes Saidi and Valipour [5], Nouri-Borujerdi [6], Promvonge and Eiasma-ard [7] and Behera et al. [8] all concluded that maximum cold-exit temperature separation was achieved for $d_c/D = 0.50$. In the current study $d_c/D = 0.50$ was chosen as a fixed parameter.

Westley [9] carried out many experiments to optimise vortex tube performance and calculated the value of A_1/A for a given p_{01}/p_c that achieved the maximum cold-exit temperature separation. This was presented in the following form:

$$\frac{A_1}{A} = 0.156 + 0.176\left(\frac{p_{01}}{p_c}\right)^{-1} \tag{2}$$

With $p_{01}/p_c = 3.0$, this gives $A_1/A = 0.215$. In the current study $A_1/A = 0.220$ was chosen as a fixed parameter.

The vortex tube geometry has been shown to affect performance. Devade and Pise [10] experimentally compared convergent and straight-cylindrical vortex tubes by varying pressure ratio and fixing the cold mass fraction at $\varepsilon = 0.90$. They found that for pressure ratios in the range $2.0 \leq p_{01}/p_c \leq 5.0$ convergent vortex tubes generally provide significantly higher cold-gas energy separation and higher cold-exit temperature separation than straight-cylindrical vortex tubes with equivalent geometrical parameters. The same authors [11] experimentally compared divergent (divergence half-angle $0 \leq \beta \leq 5^\circ$) and cylindrical vortex tubes in terms of cold-exit temperature separation performance. They found that divergent vortex tubes gave greater cold-exit temperature separation than straight vortex tubes with otherwise identical geometry. Of the designs tested, and over the range $0.30 \leq \varepsilon \leq 0.92$, divergent vortex tubes with half-angle $\beta = 5^\circ$ provided the highest cold-exit temperature separation. Interestingly, they also found that vortex tubes with larger divergence angles ($4^\circ \leq \beta \leq 5^\circ$) produced lower cold-exit temperature separation at low cold mass fractions ($\varepsilon \leq 0.30$). There is insufficient data in the literature to whether—in general—divergent, convergent or cylindrical tubes have optimum performance. In the current study a divergent vortex tube design was chosen. This has been shown in some studies to provide higher cold-exit temperature separation than the straight-cylindrical vortex tubes and addressed a gap in the literature (comprehensive performance characterisation).

The vortex tube used in the current study had half-angle $\beta = 3^\circ$: this represents a compromise between maximising temperature separation over a wide range of ε, and maximising energy separation at the optimum performance point.

Inlet nozzle design has also been found to affect performance. Pourmahmoud et al. [12] numerically compared straight and helical inlet nozzles for a straight-cylindrical vortex tube. They found that an inlet configuration with three helical nozzles provided greater hot-gas and cold-gas energy separation (cold-gas energy separation was about 5% higher at $\varepsilon = 0.67$) than an inlet configuration with three straight nozzles. Eiamsa-ard [13] designed the "snail entry" (four nozzles) and tested it experimentally for a straight-cylindrical vortex tube. Greater cold-exit temperature separation was achieved than for comparable straight tangential nozzles (cold-exit temperature separation was about 20% higher at $\varepsilon = 0.31$). Devade and Pise [11] experimentally compared straight and spiral inlet nozzles. They found that the maximum cold-exit temperature separation occurs with two spiral nozzles and $\varepsilon = 0.45$ (17% improvement over straight nozzles), however this was a local maximum, with lower temperature separation either side of this operating point. Although modest improvements appear to have been offered by unusual nozzle designs, a large body of the literature is concerned with straight tangential inlet nozzles, which are both easy to specify and reproduce, and which have broad peaks in the performance curves. For these reasons a design with six straight tangential inlet nozzles was chosen for the current study (description in Experiment and Processing).

1.2. Vortex tube operating point (free parameters)

Free parameters in the current study were the overall total-to-static pressure ratio (between inlet and cold-exit conditions) and the cold-gas mass fraction.

Kirmaci [14] showed experimentally, for a straight-cylindrical vortex tube, that cold-exit temperature separation increases steeply at low values of p_{01}/p_c (in the range 1.5–4.0), but that the rate of increase is much lower in the range $4.0 < p_{01}/p_c \leq 7.0$. The results of Agrawal et al. [15] were in broad agreement with this result. They showed experimentally, for a straight-cylindrical vortex tube, that cold-exit temperature separation increases with pressure ratio in the range $3.0 \leq p_{01}/p_c \leq 5.0$, but at a decreasing rate with

increasing pressure ratio. In the current study $p_{01}/p_c = 3.0$, 5.0 and 7.0 were chosen: this covers the range in which most open-literature results reach the asymptotic limit, and is in-line with typical lab air supply pressures (100 psi).

Many researchers have previously characterised vortex tube performance over the full range of cold-gas mass fractions, one example being the study by Stephan et al. [16], who showed experimentally that the maximum cold-exit temperature separation occurs at approximately $\varepsilon = 0.30$. The performance of the vortex tube used in the current study is characterised over the full range of cold-gas mass fractions, $0.0 < \varepsilon < 1.0$.

2. Thermodynamic analysis

The processes by which a vortex tube achieves energy separation are not fully understood but include both heat transfer (conduction down the temperature gradient) and work transfer (shear driving work down the velocity gradient). A block diagram and *T-s* chart representing the overall thermodynamic cycle, including the compression for the feed air supply, are shown in Fig. 2 and Fig. 3, respectively. In this analysis the air is treated as an ideal gas and Joule-Thomson effects are ignored (these are discussed in Data Processing and Results and Discussion). The process is as follows:

- 2–3: air is drawn from the atmosphere and compressed to the tank pressure ($p_3 = p_4 = 28$ bar, in this system, where this pressure is arbitrary and sufficiently high to achieve a wide range of experimental conditions). This process is assumed to be both adiabatic and isentropic. The tank entry temperature is T_{03}.
- 3–4: isobaric cooling to ambient temperature ($T_{04} = 290$ K, in this system).
- 4–1: the air is throttled (isenthalpic process; $T_{01} = T_{04}$) to the required vortex tube inlet pressure (e.g. $p_{01} = 7.0$ bar, in this system).
- 1–2: in a *perfectly inefficient* vortex tube, the flow is effectively throttled back to atmospheric pressure ($p_{02} = 1.0$ bar). This process is isenthalpic so $T_{02} = T_{01}$. In the real vortex tube, the flow is split into cold (c) and hot (h_1 and h_2) streams at near-atmospheric pressures ($p_c \approx p_{atm}$) and at a pressure dictated by the set point of the hot-exit ball valve ($p_{h_1} > p_{atm}$), respectively. Beyond the hot-exit ball valve the flow is throttled (isenthalpic process) to atmospheric pressure (h_2). These processes are shown in Fig. 3. The relationship between these pressures is discussed in Experiment and Processing. The streams have outlet temperatures T_{0c} and T_{0h}, respectively, separated ($T_{0c} \neq T_{0h}$) through heat and work transfer processes within the tube. These processes are marked $\dot{Q}$ and $\dot{W}$ in Fig. 2. The mass average temperature of these streams is still T_{02}. For the purpose of defining an efficiency parameter (next section) an equivalent isentropic expansion process 1–c′ is defined. This is also marked in Fig. 3.

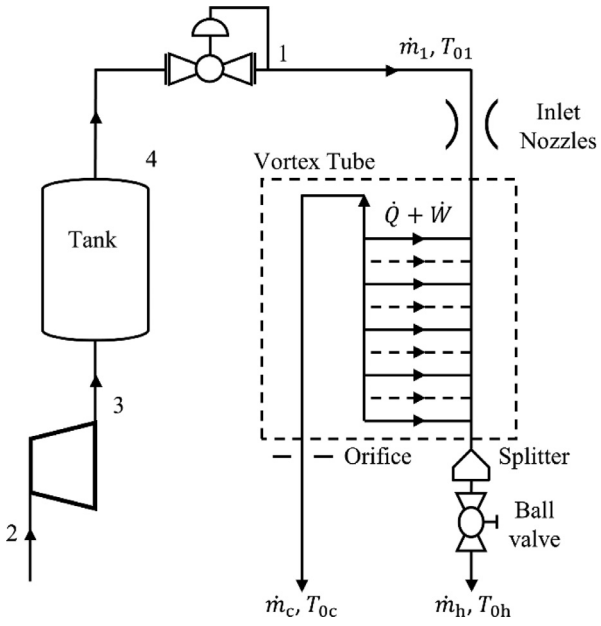

Fig. 2. Block-diagram representation of the process.

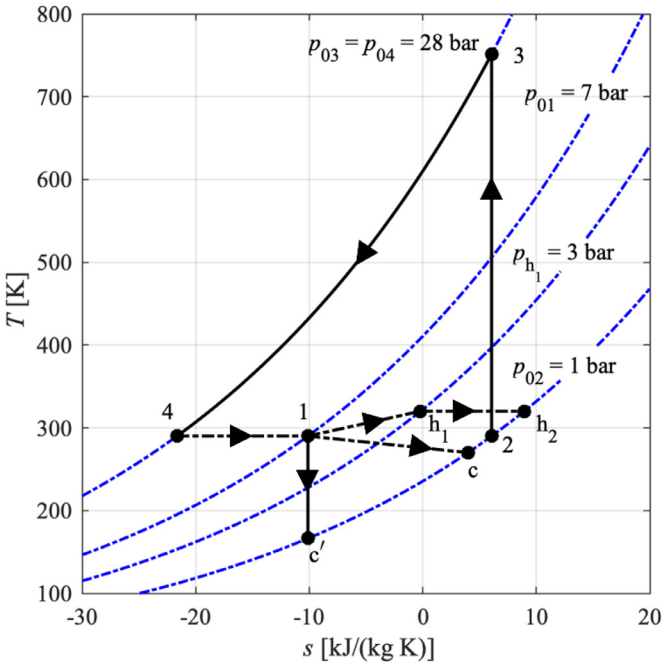

Fig. 3. Thermodynamic cycle on *T-s* diagram ($p_{01}/p_c = 7.0$).

3. Performance metrics

The performance metrics used to present the vortex tube experimental results are now discussed. First, definitions of non-dimensional temperature are considered. Cold-gas and hot-gas energy separation metrics are then introduced. Finally, measures of efficiency and coefficient of performance are considered. The independent variables that set the operating point are taken to be the cold mass fraction, ε, and the overall pressure ratio, p_{01}/p_c. A third dependent variable that is set by the geometry of the vortex tube (including the cold-exit orifice diameter, and the hot-exit splitter design) is the hot-exit pressure p_h. In the next section the relationship $p_h/p_{atm} = f(p_{01}/p_c, \varepsilon)$ is established. In the following section, although the performance metrics are represented as functions of ε and p_{01}/p_c, a fixed geometry is implicitly assumed with an implied relationship $p_h/p_{atm} = f(p_{01}/p_c, \varepsilon)$.

3.1. Non-dimensional temperatures

Non-dimensional cold and hot temperatures are defined by

$$\theta_c\left(\varepsilon, \frac{p_{01}}{p_c}\right) = \frac{T_{0c}}{T_{01}} \tag{3}$$

and

$$\theta_h\left(\varepsilon, \frac{p_{01}}{p_c}\right) = \frac{T_{0h}}{T_{01}} \tag{4}$$

where T_{0c} and T_{0h} are the measured cold and hot-exit temperatures, and T_{01} is the measured inlet temperature. This parameter defines the temperature separation the device can achieve.

Noting that most of the physics of the vortex tube is governed by geometry, overall system pressure *ratio*, and the cold-gas mass fraction, but that Joule-Thomson effects scale with *absolute* pressure, temperature and pressure drop, ratios are defined with respect to corrected temperatures which take account of the Joule-Thomson effect. That is, T_{01} is replaced in Eqs. (3) and (4) with T^*_{01}, the temperature that would be achieved in an adiabatic throttling process 1, 2 (Fig. 3) taking account of the Joule-Thomson effect. Thus, corrected non-dimensional cold-exit and hot-exit temperatures are defined by

$$\theta^*_c\left(\varepsilon, \frac{p_{01}}{p_c}\right) = \frac{T_{0c}}{T^*_{01}} \tag{5}$$

and

$$\theta^*_h\left(\varepsilon, \frac{p_{01}}{p_c}\right) = \frac{T_{0h}}{T^*_{01}} \tag{6}$$

Similar corrections could be made to the other performance parameters, but—as will be shown in Results and Discussion—the magnitude of the effect is relatively small, being equal to approximately 6.3% of the mean cold-exit temperature separation $(1-\theta_c)$ and 7.4% of the mean hot-exit temperature separation $(1-\theta_h)$ over the range tested.

3.2. Non-dimensional cold-gas and hot-gas energy separation parameters

Cold-gas and hot-gas energy separation parameters are now defined (E_c and E_h, respectively) which act as a measure of the energy transferred between the cold and hot streams. The process is primarily due to work performed by viscous shear stress down the velocity gradient. The energy lost by the cold stream and gained by the hot stream is normalised by the inlet enthalpy flux giving

$$E_c\left(\varepsilon, \frac{p_{01}}{p_c}\right) = \frac{\dot{m}_c c_p (T_{01} - T_{0c})}{\dot{m}_1 c_p T_{01}} = \varepsilon(1-\theta_c) \tag{7}$$

and

$$E_h\left(\varepsilon, \frac{p_{01}}{p_c}\right) = \frac{\dot{m}_h c_p (T_{0h} - T_{01})}{\dot{m}_1 c_p T_{01}} = (1-\varepsilon)(\theta_h - 1) \tag{8}$$

where $\dot{m}_h$ is hot-exit mass flow rate and c_p is specific heat capacity at constant pressure for air.

For an adiabatic overall system at steady state conditions, with perfect measurement, these two terms are equal ($E_c = E_h$). The terms are separately defined and calculated in the current study to allow for the possibility of imperfect measurement.

3.3. Isentropic efficiency

For the purpose of the current study, isentropic efficiency is defined in two ways. In the first definition the ratio of measured cold-gas energy separation (energy lost by the cold stream) to that which would have been achieved if the cold stream were to undergo an isentropic expansion from the inlet pressure to the cold-exit pressure is taken, that is

$$\eta_1\left(\varepsilon, \frac{p_{01}}{p_c}\right) = \frac{\dot{m}_c c_p (T_{01} - T_{0c})}{\dot{m}_c c_p T_{01}\left(1 - \left(\frac{p_c}{p_{01}}\right)^{\frac{\gamma-1}{\gamma}}\right)} = \frac{1-\theta_c}{\left(1 - \left(\frac{p_c}{p_{01}}\right)^{\frac{\gamma-1}{\gamma}}\right)} \tag{9}$$

where γ is the ratio of specific heat capacities for air ($\gamma = c_p/c_v$).

In Fig. 3 the actual cold-gas energy separation process is marked by 1 to c whilst the corresponding isentropic process is marked 1 to c′. In this efficiency definition the ability of the cold stream to work on the hot stream is compared to the ability of the cold stream to perform its maximum (isentropic) work between the same pressures. The thermodynamic cost of the hot stream is ignored.

In the second definition, the ratio of cold-gas energy separation to the energy separation that would have been achieved if the *entire inlet stream* were to undergo an isentropic expansion from the inlet pressure to the cold-exit pressure is taken. That is

$$\eta_2\left(\varepsilon, \frac{p_{01}}{p_c}\right) = \frac{\dot{m}_c c_p (T_{01} - T_{0c})}{\dot{m}_1 c_p T_{01}\left(1 - \left(\frac{p_c}{p_{01}}\right)^{\frac{\gamma-1}{\gamma}}\right)} = \frac{\varepsilon(1-\theta_c)}{\left(1 - \left(\frac{p_c}{p_{01}}\right)^{\frac{\gamma-1}{\gamma}}\right)} \tag{10}$$

This definition represents the efficiency with reference to an ideal turbo-expander.

3.4. Coefficient of performance as refrigerator

For vortex tubes used as a refrigerator, the coefficient of performance, COP_c, is a measure of the decrease in enthalpy flux of the cold stream (refrigerating potential) to the work required to compress air from ambient conditions to the inlet pressure. Note that here inlet pressure is regarded as that associated with state 1 on Fig. 3 (that is 3.0, 5.0 or 7.0 bar) not state 4 (that is, 28 bar), the latter being an arbitrary value in the current system which is sufficiently high to achieve a wide range of experimental conditions. Taking the compression energy required as that associated with an *isentropic* compression of the entire inlet stream from atmospheric conditions to the inlet pressure (state 1), yields a COP equal to the efficiency defined with respect to an ideal turbo-expander: i.e. $COP_c = \eta_2$. It is more common in the literature to define the COP with respect to an *isothermal* compression of the inlet stream, however, yielding the lowest possible compression energy and the highest possible COP that would be achievable in practice, that is

$$\mathrm{COP}_c\left(\varepsilon, \frac{p_{01}}{p_c}\right) = \frac{\dot{m}_c c_p (T_{01} - T_{0c})}{\dot{m}_1 c_p \left(\frac{\gamma-1}{\gamma}\right) T_{01} \ln\left(\frac{p_{01}}{p_c}\right)} = \varepsilon \frac{\gamma}{\gamma-1} \frac{(1-\theta_c)}{\ln\left(\frac{p_{01}}{p_c}\right)} \tag{11}$$

4. Experiment and processing

Practical details of the facility design and operation, the vortex tube design, and instrumentation and data acquisition are now discussed. Details of the uncertainty analysis are given in the appendix.

4.1. Facility design and operation

A schematic of the test facility is shown in Fig. 4. The facility operates in blow-down mode from two 30 m^3 tanks initially at 28 bar. During a test, a pilot-operated pressure regulator (operable

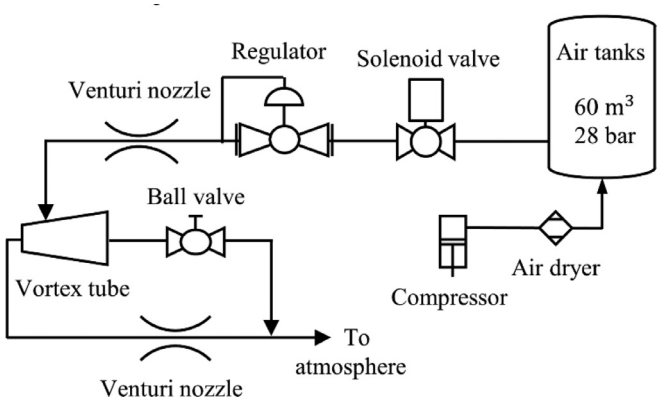

Fig. 4. Network schematic of the test facility.

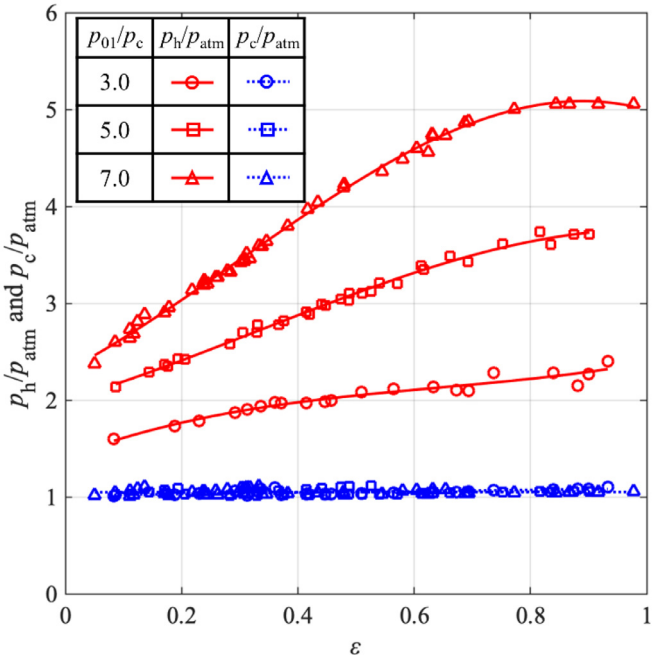

Fig. 5. Operating pressure characteristics for the vortex tube.

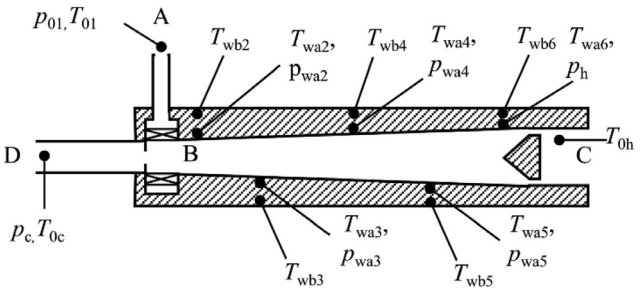

Fig. 6. Schematic of vortex tube and measurement points.

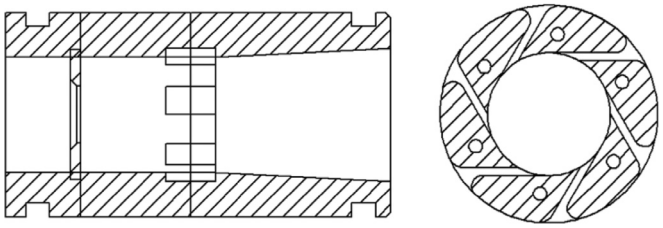

Fig. 7. Schematic of the swirler ring and cold-exit orifice.

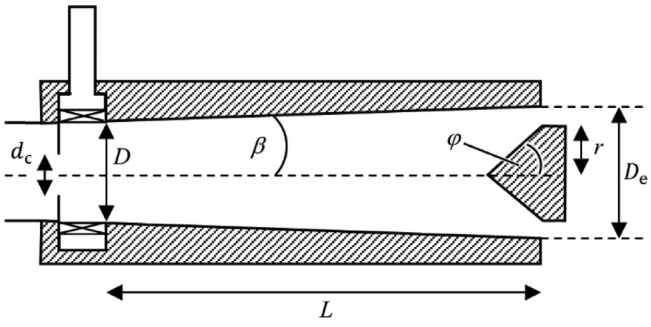

Fig. 8. Schematic of vortex tube with key parameters marked.

across a wide range of conditions) was used to maintain constant pressure, $p_{0,up}$ (typically 10–15 bar), upstream of the inlet critical venturi nozzle [17]. This pressure was set to a value to ensure that the inlet nozzle was choked, allowing the inlet mass flow rate, $\dot{m}_1$, to be measured (nozzles of throat diameter, $d_{nt} = 5.5$–7.0 mm diameter). This effectively sets a mass flow inlet boundary condition to the facility. The mass flow boundary condition (combination of inlet nozzle size and upstream pressure) dictates the nozzle ring inlet pressure, p_{01}. The test conditions used in the current study were p_{01} equal to 3.0, 5.0 and 7.0 bar. In practice p_{01} was found to be insensitive to the cold-gas mass fraction, ε, and therefore a single regulator set pressure could be used for a range of mass flow ratios. At the highest inlet pressure, a typical mass flow rate was 0.10 kg/s. This is below the recharge rate of the compressors, and therefore the tank temperature and pressure are generally relatively constant during a run.

The cold outlet mass flow rate, $\dot{m}_c$, was measured using a subsonic venturi nozzle [18] of diameter in the range 10–28 mm. The diameter was chosen to minimise the backpressure increase (maintain p_c close to atmospheric pressure) whilst maintaining adequate pressure difference for accurate measurements (details of uncertainty analysis Appendix 1). The hot-outlet mass flow rate, $\dot{m}_h$, was found by difference ($\dot{m}_h = \dot{m}_1 - \dot{m}_c$) from the two measured mass flow rates (see uncertainty analysis later). The cold-gas mass fraction was adjusted using a hand-operated ball valve downstream of the hot outlet splitter. For a fixed vortex tube design (including hot-exit splitter design) and cold-exit nozzle diameter size, there is a well-defined relationship between the vortex tube operating pressures and two principal operating parameters (i.e. the cold-gas mass fraction and the overall pressure ratio). Considering the cold-exit nozzle downstream pressure and the hot-exit splitter upstream pressure the functional forms are $p_h/p_{atm} = f(p_{01}/p_c,\ \varepsilon)$ and $p_c/p_{atm} = f(p_{01}/p_c,\ \varepsilon)$. These relationships are shown in Fig. 5. The cold nozzle downstream pressure is extremely close to atmospheric pressure over the entire range of operating conditions. The vortex tube hot-exit splitter upstream pressure, p_h, increases with both cold-gas mass fraction, ε, and the overall pressure ratio, p_{01}/p_c. The particular characteristics are a function of the entire vortex tube design including the cold-exit limiter size and hot-exit splitter design. For completeness it is noted that the static pressure at all points ($p_{wa2}, \ldots, p_{wa5}$), (see Fig. 6) was extremely similar to p_h at all operating points: i.e. the vortex tube has almost constant static pressure along the inner wall.

4.2. Vortex tube design

The tube in the current study is shown schematically in Fig. 6. The vortex tube is fed from a regulator (see Fig. 4) to inlet port A. The flow then passes through a swirler ring, B, being ejected through six tangential rectangular nozzles with a 10:1 aspect ratio at outlet. The vortex tube BC has a half-angle, β, equal to 3°, and overall length 460 mm. This gave an exit-to-inlet internal diameter ratio, $D_e/D = 3.1$. The hot-end outlet, C, has a conical splitter with half-angle $\varphi = 45°$ and ratio of outer radius to hot-exit internal diameter $r/D_e = 0.44$. The cold gas passes through a limiting orifice installed on the cold side of the swirler ring, into outlet pipe D. The walls of the vortex tube were made from steel. A schematic of the swirler ring and cold-exit orifice is presented in Fig. 7. Design parameters are summarised in Table 1 and key parameters are shown in Fig. 8.

4.3. Instrumentation and data acquisition

The sonic venturi metre was installed with upstream total pressure and total temperature measurements and downstream static pressure tappings to allow inlet mass flow rate to be determined.

Table 1
Summary of key dimensions.

Parameter	Value
Vortex tube length, L (mm)	460
Vortex tube half-angle, β (deg)	3
Half-angle of hot-exit conical splitter, φ (deg)	45
Number of inlet nozzles, N (−)	6
Ratio of combined inlet nozzle throat area to vortex tube inlet internal cross-sectional area, A_1/A (−)	0.22
Ratio of cold-exit orifice plate diameter to vortex tube inlet diameter, d_c/D (−)	0.50
Ratio of vortex tube length to inlet internal diameter, L/D (−)	20
Vortex tube exit-to-inlet internal diameter ratio, D_e/D	3.1
Vortex tube hot-splitter outer radius to exit diameter ratio, r/D_e	0.44

The bias errors were taken to be 0.10% of full-scale (First Sensor CTE8000 0–35 bara) for pressure, as quoted on the manufacturer's data sheet, and approximately 1.0 K for temperature.

The subsonic venturi downstream of the cold-exit was installed with upstream static pressure (Druck PMP-5000 0–2 bar) and total temperature measurements and a throat static pressure tapping (Druck PMP-5000 0–2 bar) to allow the cold outlet mass flow rate to be determined. The bias errors were taken to be 0.040% of full-scale (0–2 bara) for the absolute pressure sensors and approximately 1.0 K for temperature.

The nozzle ring inlet pressure and temperature (p_{01}, T_{01}) were measured with a high accuracy pressure transducer (First Sensor CTE8000 0–10 bara) and a *K*-type thermocouple. The locations are marked in Fig. 6. The bias errors were taken to be 0.10% of full-scale for pressure (0–10 bara range) and approximately 1.0 K for temperature.

The hot outlet temperature (T_{0h}) was measured at approximately 6.8r downstream of the hot-exit plane with a K-type thermocouple. The bias error was approximately 1.0 K for temperature.

The cold outlet total temperature, T_{0c}, and static pressure, p_c, were measured at approximately 15d_c downstream of the cold orifice. For the temperature measurement a rake of four thermocouples was used, giving an estimated bias error in the mean of 0.50 K. The bias error in the pressure measurement was taken to be 0.10% of full-scale (First Sensor CTE8000 0–10 bara).

To allow the data to be corrected for heat flux terms between the working gas and the walls (to render the experiment closer to an adiabatic condition), the inner and outer walls of the vortex tube were installed with five pairs of thermocouples T_{wa2}, T_{wb2} to T_{wa6}, T_{wb6}, installed very close to the inner wall and outer wall surfaces (see Fig. 6). This allowed a zero-dimensional unsteady correction method to be employed (discussed in the next section).

To understand the pressure variation within the vortex tube, four additional static pressure tappings, p_{2a} to p_{5a}, were installed in the chamber walls. p_h was measured with a static pressure tapping installed in the chamber walls a distance of 1.5r upstream of the hot-exit throat (at the outer diameter of the conical splitter). The approximate locations are marked in Fig. 6.

Data acquisition was with a Labview and National Instruments system. Data was sampled at 50 Hz in all experiments.

5. Data processing

Corrections to the experimentally measured temperature ratios for the Joule-Thomson effect and zero-dimensional transient heat flux correction to reduce experimental settling time are now discussed.

5.1. Joule-Thomson effect

To allow presentation of temperature ratios accounting for the Joule-Thomson effect (to separate out this effect) a correction term was implemented.

For air at typical ambient temperature the Joule-Thomson coefficient is approximately 0.24 K/bar [19], giving a temperature lapse of approximately $\Delta T = 1.4$ K in an adiabatic throttling process from 7.0 to 1.0 bar. When processing the data, $\Delta T(t)$ was evaluated in real time, based on the pressure difference, $\Delta p = p_{01} - p_c$. Thus, a real-time *Joule-Thomson-corrected inlet temperature* is defined by $T^*_{01}(t) = T_{01}(t) - \Delta T(t)$. This is used in Eqs. (5) and (6) to compute the corrected non-dimensional hot-exit and cold-exit temperatures, respectively. The corrected inlet temperature could be used in all the performance parameters to render them into non-dimensional groups independent of this effect. It is shown in Results and Discussion that the effect is relatively small giving an average offset $\theta^*_c - \theta_c = 0.0035$ and $\theta^*_h - \theta_h = 0.0039$. This is equivalent to offsets in η and $\mathrm{COP_c}$ of 0.0092 and 0.0032, or 6.0% and 5.9% of the mean value of these data, respectively. Because the effect is relatively small, and because *overall* performance (i.e. including Joule-Thomson effects, even though it makes it more difficult to scale results) might be taken to be of primary direct interest, complete results are presented only for the temperature ratio parameters.

5.2. Justification for zero-dimensional transient heat flux corrections

A transient heat flux correction technique was employed to correct for unsteady heat flux terms from the working gas to the vortex chamber walls. This allows accurate estimates of the steady-state (adiabatic) condition without the need to run experiments to convergence. This unsteady correction method is now described.

In the current experiment, the heat transfer between the working gas and the walls was generally positive (i.e. heat lost from the system). This is logical because the primary temperature segregation effect in the swirling flow is such that there is hot gas at the periphery (in contact with the wall, and with net flow towards the hot outlet) and cold gas towards the core (with net flow towards the cold outlet, in a contrary direction to the hot flow). The temperature gradient that is set up along the inner surface of the vortex tube is complex, but because the heat transfer *within* the working gas happens over the length of the tube, the peripheral gas generally increases in temperature towards the hot outlet.

First, a typical facility inlet temperature characteristic, $T_{01}(t)$, is considered. This is plotted in Fig. 9. Before flow is initiated ($t < -17$ s) the air in the pipe is quiescent. For the run shown, the temperature is recovering to ambient from conditions of a previous run. Flow is initiated at approximately $t = -17$ s, and there is an initial compression spike ($-17\,s < t < 0$ s). The end of the compression spike is defined to be $t = 0$. This is marked in Fig. 9. After the compression spike ($t > 0$ s) the flow follows a quasi-steady downward characteristic determined by a balance between isentropic expansion in the main tank and heat transfer to the cooling flow. This temperature trend, $T_{01}(t)$, is used to normalise data in the following plots.

Normalised temperature characteristics from a typical run are plotted in Fig. 10, in particular: the inlet temperature normalised

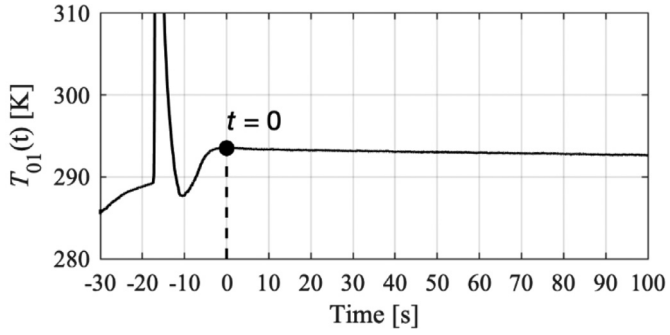

Fig. 9. Typical inlet temperature characteristic.

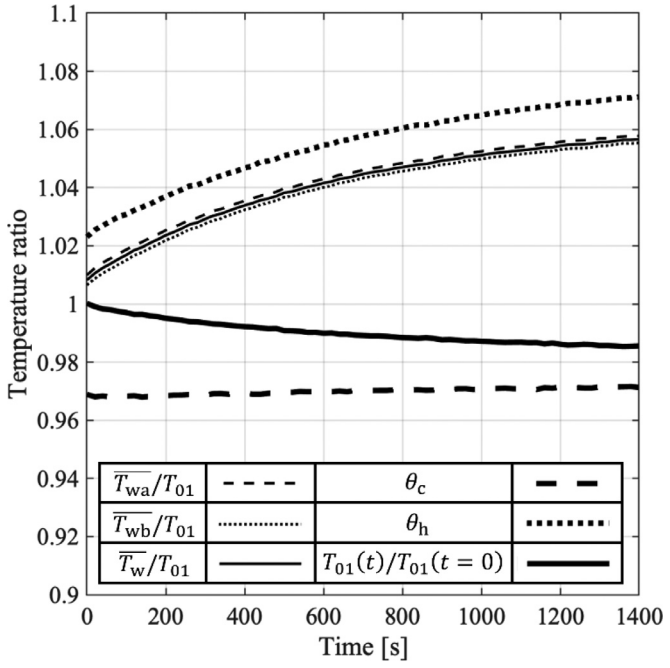

Fig. 10. Wall temperature measurements for a run with high heat flux between working gas and the wall ($p_{01}/p_c = 3.0$, $\varepsilon = 0.69$).

by the initial inlet temperature $T_{01}(t)/T_{01}(t=0)$; the normalised cold and hot-exit gas temperatures, θ_c and θ_h, respectively; the normalised average internal wall temperature $\overline{T_{wa}}/T_{01}$ (average of T_{wa2} to T_{wa6}); the normalised average external wall temperature $\overline{T_{wb}}/T_{01}$ (average of T_{wb2} to T_{wb6}); and the normalised average wall temperature $\overline{T_w}/T_{01}$ (average of T_{w2} to T_{w6}, where $T_{w2} = \frac{1}{2}(T_{wa2} + T_{wb2})$ etc.). The data are for a run with $p_{01}/p_c = 3.0$ and $\varepsilon = 0.69$, which was characteristic of a run with significant initial heat transfer between the working gas and the walls. The length of the run was 1400 s or approximately 23 min.

Looking first at the normalised inlet temperature, $T_{01}(t)/T_{01}(t=0)$, there is a quasi-steady characteristic with a lapse to approximately $T_{01}(t)/T_{01}(t=0) = 0.986$. The cold-exit gas temperature normalised by the real time inlet temperature, θ_c, is extremely stable, varying by only 0.0022 (or approximately 5.9% of the mean value of $1-\theta_c$) over the run time. In contrast the normalised hot-exit gas temperature, θ_h, rises on a quasi-exponential trend varying between $\theta_h = 1.02$ and $\theta_h = 1.07$ at the beginning and end of the run, respectively. This trend is explained by the normalised average wall temperature, $\overline{T_w}/T_{01}$, which has a similar characteristic. That is, the hot outlet response is heavily damped by the thermal mass of the wall. Even when approximately steady state conditions have been reached ($t = 1400$ s), $\theta_h(t)$ is higher

Table 2
Time constants and internal heat transfer coefficients for each zone of the vortex tube.

Zone	2	3	4	5	6
τ (s)	270	370	460	520	560
h (W/(m^2 K))	1100	740	450	320	180

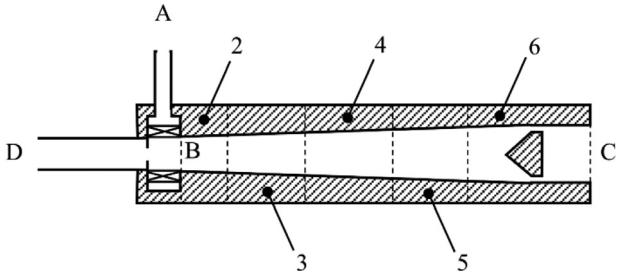

Fig. 11. Schematic diagram of vortex tube, indicating the five sections of the tube.

than $\overline{T_w}/T_{01}(t)$. Although this seems unintuitive, this is possible because the wall temperature increases along the length of the vortex tube towards the hot exit as the hot-gas energy separation advances. That is, whilst the temperature separation between T_{0h} and T_{w6} (not shown) is very small once steady state conditions have been reached, the difference between T_{0h} and *average* wall temperature is significant. The trends for $\overline{T_{wa}}/T_{01}(t)$ and $\overline{T_{wb}}/T_{01}(t)$ are almost identical to $\overline{T_w}/T_{01}(t)$, with only a very small absolute offset in temperatures. This shows that the through-wall temperature gradient is small.

Taking an *assumed step change* in driving gas temperature between the start and end points of the trend $\overline{T_w}(t)$ (0 s and 1400 s, respectively) the system is approximated as a zero-dimensional heat capacitor, for which the response to a step change in gas temperature is of form:

$$\overline{T_w}(t) = \left(\overline{T_w}(t=0) - \overline{T_w}(t=1400)\right)e^{-(t/\tau)} + \overline{T_w}(t=1400) \quad (12)$$

Finding the best-fit value of τ gives $\tau = 470$ s. This is an approximate approach for two reasons: firstly, the system inlet driving gas temperature, T_{01}, is continuously changing; secondly, the real driving gas temperature varies with distance along the tube and is therefore—locally—poorly approximated by $\overline{T_w}(t=1400)$ over most of the tube. Despite these approximations, the approach gives indicative values of interest. This time constant is large and demonstrates that it is necessary to run the system for several minutes to achieve steady state conditions, or to employ a transient heat flux correction. It is also noted that the ratio of the system time-constant to through-wall time constant is large, and therefore a zero-dimensional method is adequate.

It is possible to infer internal heat transfer coefficients by noting that for a heat capacitor $\tau = Mc_p/hA_a$, where h is internal heat transfer coefficient and A_a is the inner wall surface area. Putting in physical values for the overall system ($\tau = 470$ s, $M = 42.5$ kg, $c_p = 400$ J/(kg K) and $A_a = 0.09$ m^2) yields $h = 400$ W/(m^2 K). It is possible to do this for each of the five sections of tube yielding the results in Table 2. The sections are marked on Fig. 11.

Here it is interesting to see that the heat transfer coefficients decrease strongly and monotonically with axial distance. This is most likely caused by a decrease in tangential velocity with axial distance. Interestingly, the downward trend based on *real local temperature* would be even more severe than that implied by this method, which assumed constant gas temperature throughout the tube (in the real system temperature separation is increasing with axial distance).

Asymptotic temperatures, $T_{w2}(t = 1400\text{ s})$ to $T_{w6}(t = 1400\text{ s})$ (shown in Fig. 12), increase steeply and monotonically between

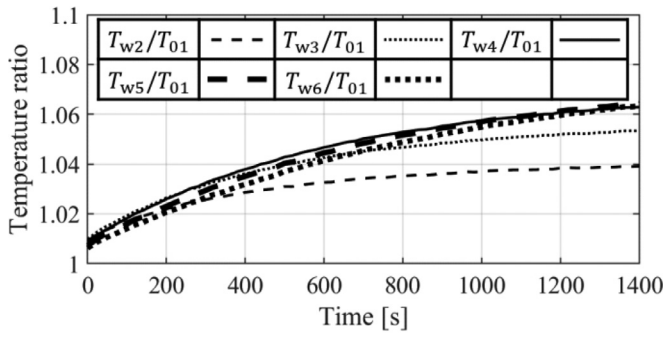

Fig. 12. Wall temperature measurements for zone 2 – 6 for a run with high heat flux between working gas and the wall ($p_{01}/p_c = 3.0$, $\varepsilon = 0.69$).

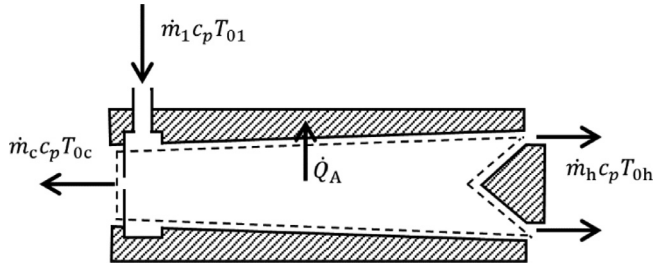

Fig. 13. Control volume for the system transient heat transfer analysis for the system.

$T_{w2}(t = 1400\,\text{s})$ and $T_{w4}(t = 1400\,\text{s})$ and are essentially constant between $T_{w4}(t = 1400\,\text{s})$ and $T_{w6}(t = 1400\,\text{s})$. The plateau in asymptotic wall temperature after a certain axial length suggests additional vortex tube length would not improve performance.

5.3. Transient heat flux correction

Implementation of a transient heat flux correction—based on overall energy balance for the system—to account for unsteady heat transfer between the flow and the walls is now discussed.

A control volume representing the vortex tube system is shown in Fig. 13.

There are three flow-based enthalpy fluxes of interest, associated with the inlet flow, $\dot{m}_1 c_p T_{01}(t)$, the hot gas exit flow, $\dot{m}_h c_p T_{0h}(t)$, and the cold gas exit flow, $\dot{m}_c c_p T_{0c}(t)$. There are, in addition, two heat fluxes of interest, a forced convention term between the working gas and the walls, $\dot{Q}_A$, and a free convention term between the walls and the environment, $\dot{Q}_B$. The overall energy balance *for the fluid* is represented by

$$\dot{m}_1 c_p T_{01}(t) = \dot{m}_c c_p T_{0c}(t) + \dot{m}_h c_p T_{0h}(t) + \dot{Q}_A(t) + \dot{Q}_R(t) \tag{13}$$

where $\dot{Q}_R(t)$ is an instantaneous residual heat flux, which arises due to measurement error (particular sensitivity to cold-exit mass flow rate and hot-exit total temperature measurements). The heat flux absorbed by the walls (e.g. Fig. 10 data), $\dot{Q}_C(t)$, is equal to the difference $\dot{Q}_A(t) - \dot{Q}_B(t)$. That is

$$\dot{Q}_A(t) - \dot{Q}_B(t) = M_2 c_p \frac{dT_{w2}(t)}{dt} + \ldots + M_6 c_p \frac{dT_{w6}(t)}{dt} = \dot{Q}_C(t) \tag{14}$$

where M_2 to M_6 are the wall mass elements (stations 2–6 in Fig. 11), and $\dot{Q}_C(t)$ is the *net heat flux* into the walls. The natural convection heat flux $\dot{Q}_B(t)$ was calculated using the correlations of mean surface Nusselt number [20] for a heated horizontal cylinder, of form

$$\overline{\text{Nu}}_f = C(\text{Gr}_f \text{Pr}_f)^m \tag{15}$$

where, Gr_f is Grashof number and Pr_f is Prandtl number (both are evaluated at the mean film temperature), and—for the conditions in this experiment—C and m take values 0.53 and 0.25, respectively [20]. Representing $\dot{Q}_B(t)$ as the sum over five wall elements, this term can be expressed as

$$\dot{Q}_B(t) = \sum_{j=2}^{6} \frac{k_{fj}\text{Nu}_{fj}A_{bj}}{D_b}\left(T_{wbj}(t) - T_{amb}\right) \tag{16}$$

where A_{bj} and $T_{wbj}(t)$ represent the individual outer wall surface areas and associated wall temperatures, and k_{fj} and Nu_{fj} are the thermal conductivity and Nusselt number evaluated at the mean film temperature for each zone. D_b is the outer diameter of the vortex tube ($D_b = 125\,\text{mm}$) and T_{amb} is the environmental temperature. Rewriting Eq. (13) using Eq. (14), and evaluating the terms at a particular time for each run (chosen so the operating point is relatively steady; not made explicit in the following equations) the inlet enthalpy flux can be expressed as

$$\dot{m}_1 c_p T_{01} = \dot{m}_c c_p T_{0c} + \dot{m}_h c_p T_{0h} + \dot{Q}_B + \dot{Q}_C + \dot{Q}_R \tag{17}$$

This is a condition for instantaneous enthalpy flux balance for the fluid control volume.

5.4. Energy balance at extrapolated adiabatic condition

An ideal experiment would be run to steady state conditions, so that terms $\dot{Q}_B$ and $\dot{Q}_C$ in Eq. (17) tend to zero. In an experiment with low measurement uncertainty $\dot{Q}_R$ would also be approximately zero. In many practical experiments, this is not possible, however, and it is helpful to define corrected temperatures (accounting for unsteady heat flux terms from the fluid) at an *extrapolated adiabatic condition*. These temperatures are referred to as T'_{0c} and T'_{0h}. To do this it is necessary to apportion the unsteady heat flux term (between fluid and walls) between the hot and cold streams. A method for doing this is now described.

Corrected cold-exit and hot-exit temperatures are defined by

$$T'_{0c} = T_{0c} + k_1 \frac{\left(\dot{Q}_B + \dot{Q}_C\right)}{\dot{m}_c c_p} \tag{18}$$

and

$$T'_{0h} = T_{0h} + (1 - k_1)\frac{\left(\dot{Q}_B + \dot{Q}_C\right)}{\dot{m}_h c_p} \tag{19}$$

where k_1 is a constant that determines how the unsteady heat flux is split between cold-exit and hot-exit streams. An optimisation approach is used to define k_1, as described in Appendix 2. Although not explicitly shown in Eqs. (18) and (19), in this method k_1 is a function of ε to improve the quality of the optimisation.

To demonstrate the utility of the approach, corrected ($\theta'_c = T'_{0c}/T_{01}$ and $\theta'_h = T'_{0h}/T_{01}$) and uncorrected ($\theta_c$ and θ_h) cold-exit and hot-exit gas temperatures are plotted for a typical run in Fig. 14 (same run as discussed in context of Fig. 10). In this run there was a step change to a single operating point with no further change in operating point.

As discussed in the context of Fig. 10, θ_h is time-varying with a time constant of approximately 540 s, and an increase of 0.046 (or 86% of the mean value of $1 - \theta_h$) over the period of the run. Implementing the transient heat flux correction technique yields θ'_h which is significantly more stable, with a lapse of only 0.0121 (approximately 15% of the mean value of $1 - \theta'_h$) over the duration of the run. The improvement in *stability* is approximately a factor of 5.7. Evaluating θ'_h at $t = 300$ s (marked in Fig. 14) yields a value which is within 0.46% of the settled value: an error in energy separation (proportional to $1 - \theta'_h$) of 6.2%. It is noted that the settled values of θ'_h and θ_h are different by an amount corresponding to 14% of the energy separation, underlining the importance of accounting for heat flux at the surfaces of the fluid control volume. In this example, the correction function is such that no correction is applied to the cold stream, so the trends for θ_c and θ'_c

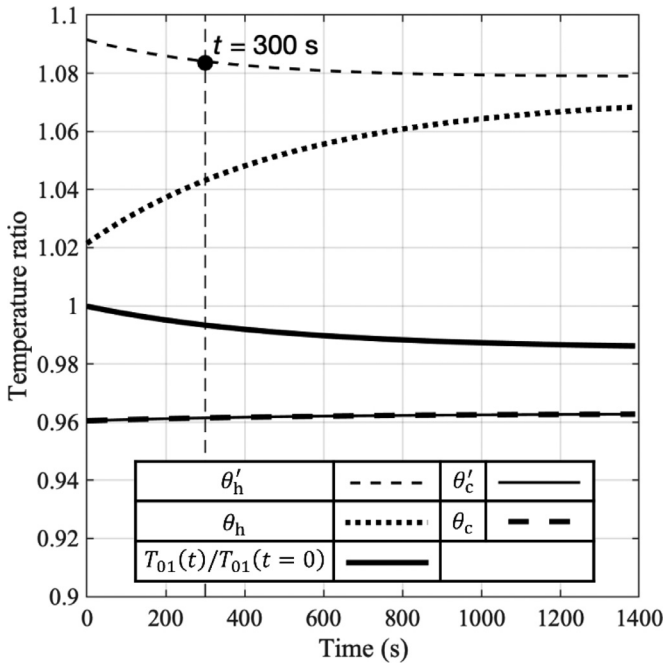

Fig. 14. Corrected and uncorrected non-dimensional exit temperatures after a step change in operating point ($p_{01}/p_c = 3.0$, $\varepsilon = 0.69$).

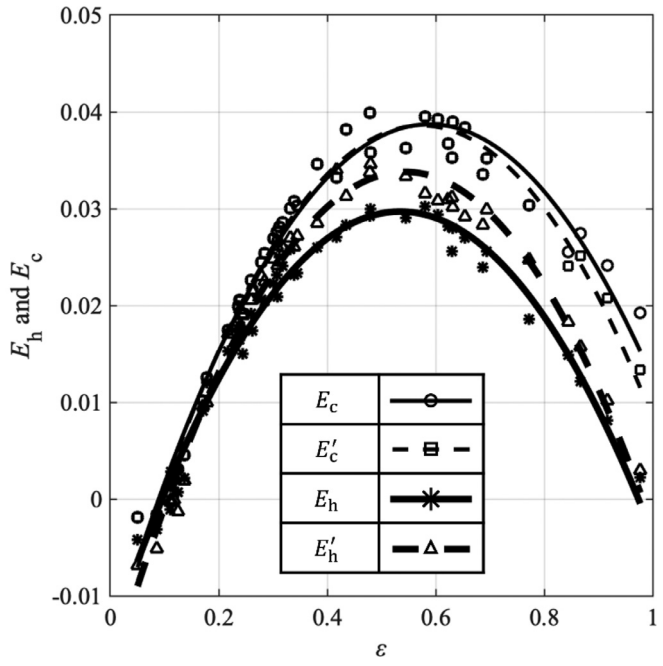

Fig. 15. Corrected and uncorrected cold-gas and hot-gas energy separation parameters as a function of ε for $p_{01}/p_c = 7.0$.

are identical. It is noted that other than for values of ε approaching unity, the heat flux correction primarily affects the hot stream, which is in more intimate contact with the wall. This is discussed in Appendix 2.

The experimental procedure adopted was to run for 300 s at a single operating point, then make small changes in operating point with a dwell period of 60 s between each. Taking data in this way, the average value of $\dot{Q}_c$ was 9.8% of the average value of cold-gas energy separation, $\dot{m}_c c_p(T_{01} - T_{0c})$ across all data, with $\dot{Q}_C$ positive (expected because hot fluid is in contact with the walls) and increasing with ε (expected because θ_h increases as ε increases). The average value of $\dot{Q}_B$ was 0.16% of average value of the cold-gas energy separation across all data. The conclusion is that whilst it is necessary to perform these corrections, the correction can be performed with reasonable accuracy.

To demonstrate the impact of the correction the corrected and uncorrected cold-gas and hot-gas energy separation parameters ($E_c = \varepsilon(1-\theta_c)$, $E'_c = \varepsilon(1-\theta'_c)$, $E_h = \varepsilon(1-\theta_h)$ and $E'_h = \varepsilon(1-\theta'_h)$) are plotted in Fig. 15. Both the raw data and second-order polynomial fits are presented for the case with pressure ratio, $p_{01}/p_c = 7.0$.

Looking first at the characteristics for E_c and E'_c, they are very similar for $0.00 < \varepsilon \leq 0.55$. This is the result of $k_1(\varepsilon)$ being set equal to zero in the range $0.0 < \varepsilon \leq 0.78$. The function $k_1(\varepsilon)$ results from the best fit to unsteady data, and is discussed in Appendix 2, but having low values $k_1(\varepsilon)$ for $\varepsilon \ll 1$ is in line with the physical intuition that in this range the cold gas has minimal direct interaction with the wall. For $\varepsilon > 0.55$, E'_c is lower than E_c (heat flux to the wall from the gas), gradually reducing to $E'_c = 0.75E_c$ for $\varepsilon = 0.98$. In the limit $\varepsilon \to 1$, $k_1(\varepsilon) \to 1$, an obvious physical constraint because there is no outflow from the hot exit.

Now consider the characteristics of E_h and E'_h. In the range $0.15 < \varepsilon \leq 0.60$ E'_h is, on average, 10% higher than E_h (heat flux to the wall from the gas). In this range $k_1(\varepsilon) > 0.95$, a result that is physically justified because peripheral gas leaving through the hot exit is in most intimate contact with the wall. For $\varepsilon > 0.60$, both E_h and E'_h converge to approximately 0, a result that is expected because of the term $1 - \varepsilon$ in Eq. (8).

In an ideal experiment (no error) run to convergence (no heat flux to walls), the curves for E_c and E_h would follow identical trends (enthalpy balance argument). The separation of these curves in Fig. 15 indicates either measurement error, or non-convergence or both. In the range $0.20 < \varepsilon \leq 0.80$, E_c and E_h differ by on average 24% of the local value of E_c. Application of the transient correction gives curves E'_c and E'_h, which differ by on average 14% of the local value of E'_c. That is, application of the unsteady correction closes the gap by approximately 42%. This demonstrates both the importance and the utility of performing the unsteady correction. The curves for E'_c and E'_h are not identical in our experiment because of finite measurement error.

In the analysis of performance parameters Eqs. (3)–((11)) that follows, the corrected exit temperatures T'_{0c} and T'_{0h} Eqs. (18) and ((19)) were used in place of T_{0c} and T_{0h}. With this change of variables, the parameters $\theta_c, \theta_h, E_c, E_h, \eta_1, \eta_2, \mathrm{COP}_c$ become $\theta'_c, \theta'_h, E'_c, E'_h, \eta'_1, \eta'_2, \mathrm{COP}'_c$.

5.5. Note on the form of best-fit

In an ideal experiment with no measurement error (and corrected for—small—Joule Thomson effect) both E_c and E'_c would converge to 0 in the limit $\varepsilon \to 0$ (note the multiplier ε in Eq. (7)). In the current experiment data is only taken to a lower limit $\varepsilon \sim 0.050$, however, and E_c and E'_c pass through 0 at approximately $\varepsilon \sim 0.100$. Although the behaviour is superficially surprising, it is unclear whether it results from measurement error or a turning point in the range $\varepsilon < 0.050$. For this reason, the second order fits are not constrained to pass through $E_c = 0$ and $E'_c = 0$ at $\varepsilon = 0$.

In similar manner, and under the same conditions, it is expected that $E_h \to 0$ and $E'_h \to 0$ as $\varepsilon \to 1$ (note the multiplier $1 - \varepsilon$ in Eq. (8)). This condition is, in fact, almost precisely met by the data, but because of the possibility of measurement error the second order fit is unconstrained.

Consider also the two limits at which there can be no energy separation. Firstly, $E'_c \to 0$ for $\varepsilon \to 1$, because (neglecting the Joule Thomson effect) $\theta_c \to 1$, and $1 - \theta_c \to 0$ (Eq. (7)) in the limit of no outflow from the hot end. Secondly, $E'_h \to 0$ for $\varepsilon \to 0$, because (neglecting the Joule Thomson effect) $\theta_h \to 1$, and $\theta_h - 1 \to 0$ (Eq. (8)) in the limit of no outflow from the cold end. In these limits finite error in temperature measurement is a real concern, so the best-fit lines are unconstrained.

6. Results and discussion

Comprehensive performance curves are now presented for a divergent vortex tube operating at three overall total-to-static pressure ratios: $p_{01}/p_c = 3.0$, 5.0 and 7.0. Seven non-dimensional performance parameters, corrected for transient heat flux are considered: the non-dimensional outlet temperatures, θ'_c and θ'_h; the non-dimensional cold-gas and hot-gas energy separation, E'_c and E'_h; the isentropic efficiencies, η'_1 and η'_2; and the coefficient of performance of the vortex tube, COP'_c. In all the characteristic plots that follow both raw data at individual operating points, and either second-order (E'_c and E'_h) or third-order (θ'_c, θ'_h, η'_1, η'_2 and COP'_c) polynomial best fit curves for each pressure ratio are presented. Typical values of uncertainty in all performance parameters can be found in Appendix 1.

6.1. Non-dimensional exit temperatures

Characteristics of non-dimensional outlet temperatures are shown in Fig. 16 as a function of ε and pressure ratio. The cold-exit temperature separation (variation from unity) peaks between approximately $\varepsilon = 0.35$ and $\varepsilon = 0.45$, and increases strongly with pressure ratio between $p_{01}/p_c = 3.0$ and 5.0, then increases weakly between $p_{01}/p_c = 5.0$ and 7.0. At the points of maximum temperature separation the non-dimensional cold-exit temperatures are $\theta'_c = 0.94$, 0.92 and 0.91 for $p_{01}/p_c = 3.0$, 5.0 and 7.0, respectively.

The hot-exit temperature separation increases approximately linearly with ε, and increases fairly strongly with pressure ratio between $p_{01}/p_c = 3.0$ and 5.0, then increases weakly between $p_{01}/p_c = 5.0$ and 7.0. At the points of maximum temperature separation, the non-dimensional hot-exit temperatures are $\theta'_h = 1.10$, 1.11 and 1.13 for $p_{01}/p_c = 3.0$, 5.0 and 7.0, respectively (note these values are from short extrapolations from the best fit curve).

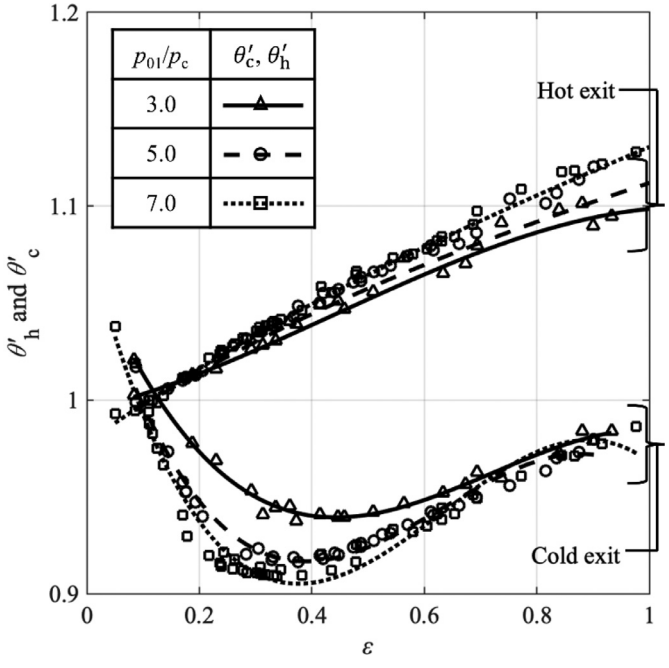

Fig. 16. Non-dimensional outlet temperatures as a function of ε and pressure ratio.

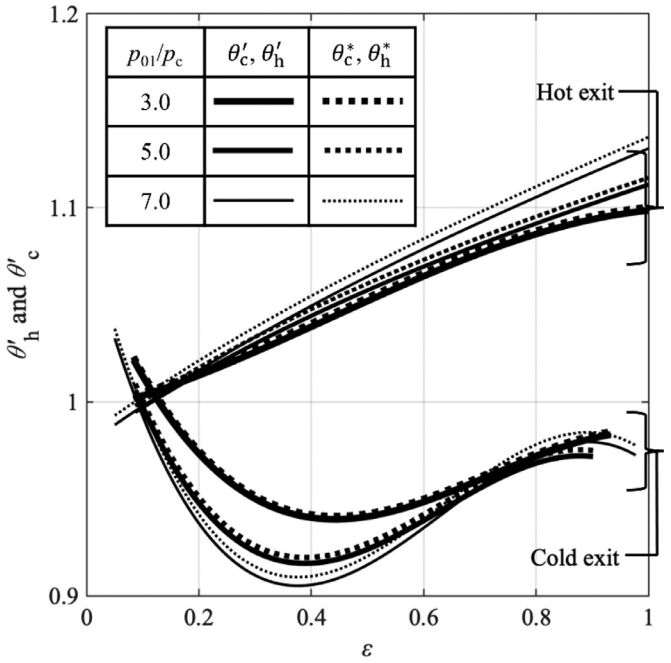

Fig. 17. Effect of Joule-Thomson correction on non-dimensional exit temperatures.

To understand the sensitivity to the Joule-Thomson effect θ'_c and θ'_h are compared with corrected quantities θ^*_c and θ^*_h (note that T'_{0c} and T'_{0h} were used in place of T_{0c} and T_{0h} in Eqs. (3)–(6) to compute θ'_c, θ'_h, θ^*_c and θ^*_h, respectively) in Fig. 17. Raw data points have been omitted for clarity. In the range $0.05 < \varepsilon < 0.98$, the mean offsets $\theta^*_c - \theta_c$ were 0.0016, 0.0031 and 0.0046 for $p_{01}/p_c = 3.0$, 5.0 and 7.0, respectively. Corresponding offsets for $\theta^*_h - \theta_h$ were 0.0017, 0.0035 and 0.0051. Looking at the temperature *separation* parameters $1 - \theta_c$ and $1 - \theta_h$, the Joule-Thomson correction is equivalent to offsets (overall mean over all ε and p_{01}/p_c tested) of 6.3% and 7.5%, respectively.

Whilst vortex tube physics is governed primarily by the geometry, overall pressure *ratio* and cold mass fraction, the Joule-Thomson effect scales with *absolute* pressure, temperature and pressure drop. To fully normalise the data, it would make sense to perform a Joule-Thomson correction, to render the performance parameters in forms that are independent of the Joule-Thomson effect, such that predictions could be made for any particular absolute pressure, temperature and pressure drop of interest. It can be seen from Fig. 17 that accounting for the Joule-Thomson effect has the consequence of underpredicting the cooling effect in many practical applications. Whilst this may be desirable to make the data as portable as possible between operating conditions, many industrial air supplies operate at pressures similar to those used in the current experiments. This relatively small correction is therefore omitted in all the analysis that follows. That is, the inlet temperature is taken as T_{01} in Eqs. (7)–(11), not T^*_{01}. In scaling to different absolute conditions, a double-correction for the Joule-Thomson effect should be accounted for.

6.2. Non-dimensional cold-gas and hot-gas energy separation

Characteristics for the cold-gas and hot-gas energy separation parameters, E'_c and E'_h, are shown as functions of ε and pressure ratio in Fig. 18 and Fig. 19, respectively.

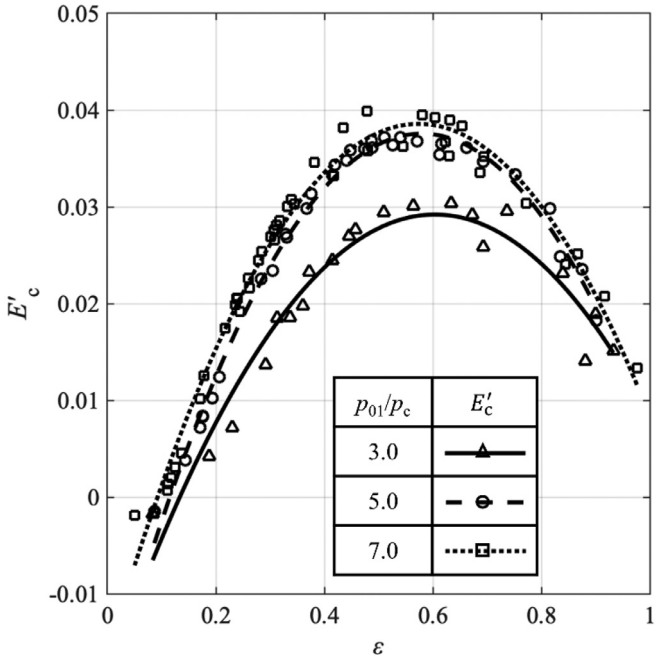

Fig. 18. Cold-gas energy separation parameter E_c as a function of ε and pressure ratio.

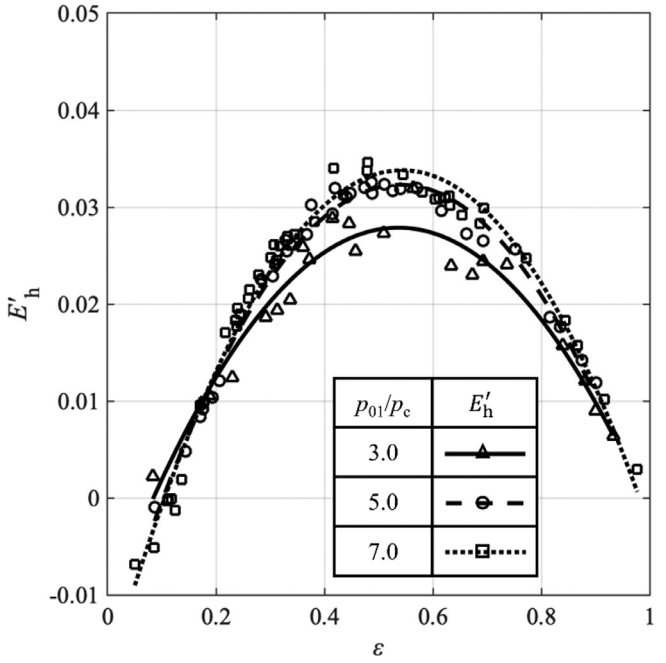

Fig. 19. Hot-gas energy separation parameter E_h as a function of ε and pressure ratio.

The general forms are parabolic, with maxima close to $\varepsilon = 0.5$. The trends are for increasing energy separation with increasing pressure ratio. Trends for E'_c and E'_h at a given pressure ratio are similar to each other, and therefore close to the result one would expect in a system with no measurement error or heat transfer (from the gas to the wall). For $p_{01}/p_c = 3.0$, 5.0 and 7.0, E'_c has maximum values 0.029, 0.038 and 0.039 at $\varepsilon = 0.60$, 0.58 and 0.57, respectively. The corresponding maximum values of E'_h are 0.028, 0.032 and 0.034 at $\varepsilon = 0.53$, 0.54 and 0.54. The maximum energy lost by the cold stream and gained by the hot stream due to viscous shear stress and heat transfer is of order 3.5% of the inlet enthalpy flux.

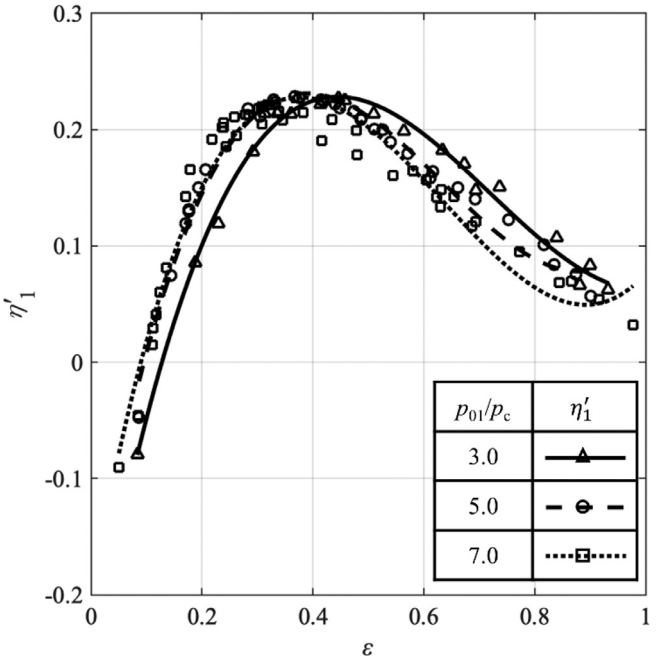

Fig. 20. Isentropic efficiency referenced to the cold-gas expansion, η'_1, as a function of ε and pressure ratio.

6.3. Isentropic efficiency referenced to cold-gas expansion

The isentropic efficiency referenced to the cold-gas expansion, η'_1, is plotted in Fig. 20 as a function of ε and pressure ratio.

The trends are quasi-parabolic in shape with maxima in the range $0.37 < \varepsilon < 0.44$. In the range $0.00 \leq \varepsilon \leq 0.40$, η'_1 increases slightly with increasing pressure ratio, and in the range $0.40 \leq \varepsilon \leq 1.00$, η'_1 *decreases* slightly with increasing pressure ratio. At high cold-gas mass fractions, although a greater temperature drop between inlet and cold exit is achieved at higher pressure ratio (see Fig. 16) this is outweighed by the increased cost of pumping the fluid to the inlet pressure. For $p_{01}/p_c = 3.0$, 5.0 and 7.0, the maximum values of η'_1 are 0.23, 0.23 and 0.23 at $\varepsilon = 0.44$, 0.39 and 0.38. At the point of maximum efficiency, the cold-gas energy separation (energy lost by the cold stream) is roughly 20% of that which would be achieved if the cold stream were to undergo an isentropic expansion from the inlet pressure to the cold-exit pressure.

6.4. Isentropic efficiency referenced to inlet stream expansion

The isentropic efficiency referenced to the inlet-gas expansion, η'_2, is plotted in Fig. 21 as a function of ε and pressure ratio. This definition represents the efficiency with reference to an ideal turbo-expander. The trends are—again— quasi-parabolic in shape with maxima in the range $0.56 < \varepsilon < 0.63$. In the range $0.00 \leq \varepsilon \leq 0.40$, η'_2 is insensitive to pressure ratio, and in the range $0.40 \leq \varepsilon \leq 1.00$, η'_2 *decreases* slightly with increasing pressure ratio. For high cold-gas mass fractions, the same mechanism (cost of pumping cold gas) can be taken to account for the decrease in efficiency. In this definition the maximum efficiency point is a compromise between high cold mass fraction and high cold-exit temperature separation. For $p_{01}/p_c = 3.0$, 5.0 and 7.0, the maximum values of η'_2 are 0.11, 0.10 and 0.091 at $\varepsilon = 0.62$, 0.58 and 0.56, respectively. At the point of maximum efficiency, the cold-gas energy separation (energy lost by the cold stream) is roughly 10% of the energy

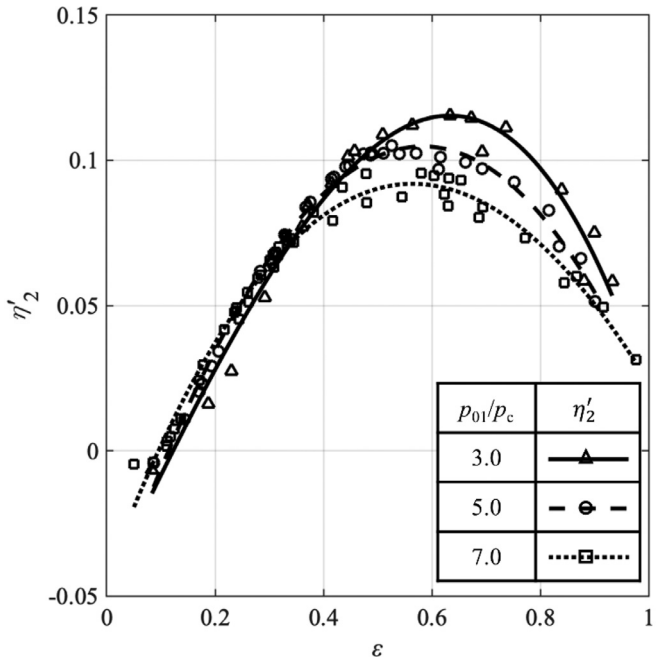

Fig. 21. Isentropic efficiency referenced to the inlet-gas expansion, η_2', as a function of ε and pressure ratio.

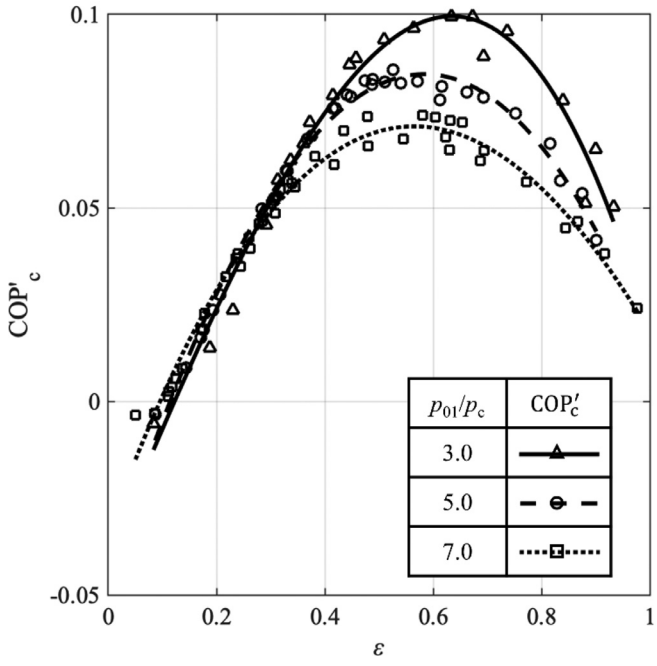

Fig. 22. Coefficient of performance for vortex tube acting as a refrigerator, COP_c, as a function of ε and pressure ratio.

separation that would have been achieved if the *entire inlet stream* were to undergo an isentropic expansion from the inlet pressure to the cold-exit pressure.

6.5. Coefficient of performance acting as refrigerator

The coefficient of performance for a vortex tube acting as refrigerator, COP_c is shown in Fig. 22 as a function of ε and pressure ratio. The characteristics are quasi-parabolic with maxima in the range $0.56 < \varepsilon < 0.63$. In the range $0.0 < \varepsilon \leq 0.35$, the COP_c characteristics are almost identical at all three pressure ratios. In the range $0.35 < \varepsilon \leq 1.0$, COP_c decreases with increasing pressure ratio. The improvement in cold-exit temperature separation achieved at higher pressure ratios is outweighed by the increased cost of compressing gas to the inlet condition. For $p_{01}/p_c = 3.0$, 5.0 and 7.0, the maximum values of COP_c are 0.097, 0.084 and 0.071 at $\varepsilon = 0.63$, 0.58 and 0.56, respectively. The refrigerating potential is approximately 10% of the minimum work required to compress air from ambient conditions to the inlet pressure.

7. Conclusions

A detailed experimental study of the performance characteristics of a divergent vortex tube has been conducted. The performance is presented in terms of: non-dimensional temperature separation; cold-gas and hot-gas energy separation; efficiency; and coefficient of performance acting as a refrigerator. The utility of these metrics is discussed, as are improved experimental methods including a transient heat flux correction, and the impact of Joule-Thomson effects on non-dimensional performance metrics. The key conclusions are:

(a) *Temperature separation* (θ_c' and θ_h') increases with overall pressure ratio with peak non-dimensional cold temperatures $\theta_c' = 0.94$, 0.92 and 0.91, at pressure ratios $p_{01}/p_c = 3.0$, 5.0 and 7.0, respectively. The lowest cold-exit temperature (0.91) was obtained at a cold-gas mass fraction of $\varepsilon = 0.34$. For inlet air at room temperature this corresponds to a temperature deficit of approximately 26.1 K. Peak non-dimensional hot-gas exit temperatures of $\theta_h' = 1.09$, 1.11 and 1.13 were achieved for $p_{01}/p_c = 3.0$, 5.0 and 7.0, respectively, these peaks occurring at a cold-gas mass fraction of unity ($\varepsilon = 1.00$).

(b) *Non-dimensional cold-gas and hot-gas energy separation* (E_c' and E_h') increased with increasing pressure ratio. For $p_{01}/p_c = 3.0$, 5.0 and 7.0, E_c' has maximum values 0.029, 0.037 and 0.038 at $\varepsilon = 0.60$, 0.58 and 0.57, respectively. The corresponding maximum values of E_h' are 0.028, 0.032 and 0.034 at $\varepsilon = 0.53$, 0.54 and 0.54. The maximum energy lost by the cold stream and gained by the hot stream due to viscous shear stress and heat transfer is of order 3.5% the inlet enthalpy flux. Small differences between the trends for E_c' and E_h' were attributed to experimental error.

(c) *Isentropic efficiency referenced to cold gas expansion* (η_1') had quasi-parabolic trends with cold-gas mass fraction (relatively insensitive to pressure ratio) with maxima (at the three pressure ratios tested) equal to approximately 0.23 for cold-gas mass fractions of approximately 0.4. The peak cold-gas energy separation was roughly 20% of that which would be achieved if the cold stream were to undergo an isentropic expansion from the inlet pressure to the cold-exit pressure.

(d) *Isentropic efficiency referenced to inlet stream expansion* (η_2') was relatively insensitive to pressure ratio with peak values of 0.11, 0.10 and 0.091 at $\varepsilon = 0.62$, 0.58 and 0.56, respectively. This can be thought of as representing the efficiency with reference to an ideal turbo-expander, with the maximum efficiency point being a compromise between high cold mass fraction and high cold-exit temperature separation. At peak efficiency, the cold-gas energy separation was roughly 10% of the energy separation that would have been achieved if the *entire inlet stream* were to undergo an isentropic expansion from the inlet pressure to the cold-exit pressure.

(e) *Coefficient of performance* for the vortex tube acting as refrigerator had quasi-parabolic trends with maxima in the range $0.56 < \varepsilon < 0.63$, with maximum values decreasing with pressure ratio. The improvement in cold-exit temperature separation achieved at higher pressure ratios is outweighed by the increased cost of compressing gas to the inlet condition. Maxi-

mum values of COP_c were in the range 0.071–0.097. The refrigerating potential was approximately 10% of the minimum work required to compress air from ambient conditions to the inlet pressure.

Declaration of Competing Interest

The authors declare that they have no known competing financial interests or personal relationships that could have appeared to influence the work reported in this paper.

CRediT authorship contribution statement

James Cartlidge: Conceptualization, Methodology, Software, Formal analysis, Writing – original draft. **Nafiz Chowdhury:** Investigation, Writing – original draft. **Thomas Povey:** Conceptualization, Writing – review & editing, Supervision.

Acknowledgments

The authors thank Daniel Burdett, Thomas Stewardson and Alessandro Bastianello for contributions to earlier iterations of the facility test stand and vortex tube design.

Appendix 1. Uncertainty analysis

Uncertainty estimations were carried out for all performance metrics and mass flow rates. The analysis was performed for an—arbitrarily chosen—inlet pressure of 5 bar. The input parameters were set to their average values over all data for an inlet pressure 5 bar. The input parameters and corresponding percentage bias error estimates are summarised in Table 3.

Percentage bias errors in temperature and pressure measurements, discharge coefficients and nozzle throat diameters are used to evaluate percentage bias errors in $\dot{m}_1, \dot{m}_c, \dot{m}_h, \varepsilon, \eta_1', \eta_2', E_c', E_h'$ and COP_c' using RSS error propagation techniques.

Percentage bias errors (as percentage of local value) for the mass flow rates and ε are presented in Fig. 23 as a function of ε. Looking first at the inlet mass flow rate, $\dot{m}_1$, the uncertainty is approximately 0.53%. Now looking at the cold-exit mass flow rate, $\dot{m}_c$, the percentage bias error is approximately constant (1.4%) in the range $0.15 < \varepsilon \leq 1.0$, but increases rapidly for $\varepsilon < 0.15$. Steps in the characteristic arise because four distinct subsonic venturis were used in the experimental process. For the hot-exit mass flow rate, $\dot{m}_h$, the percentage bias error is less than 2.0% in the range $0.0 < \varepsilon \leq 0.60$ and rises rapidly in the range $0.60 < \varepsilon \leq 1.0$. The trend for ε is similar to that for $\dot{m}_c$ but percentage bias errors are slightly greater in magnitude because errors in both $\dot{m}_1$ and $\dot{m}_c$ affect errors in ε.

Table 3
Average values and estimated errors for input parameters ($p_{01}/p_c = 5.0$).

	Value	Estimated bias error (%)
Sonic venturi		
C_d	0.99	± 0.30
d_{nt} (mm)	5.50	± 0.18
$p_{0,\,up}$ (bara)	15.29	± 0.23
$T_{0,\,up}$ (K)	289.00	± 0.12
Subsonic venturi		
C_d	0.98	± 1.20
d_{nt} (mm)	15.00	± 0.07
p_{up} (bara)	1.05	± 0.08
p_{nt} (bara)	0.65–1.05	0.19–0.31
$T_{0,\,up}$ (K)	276.00	± 0.36
Vortex tube		
T_{0c}'(K)	271.00	± 0.18
p_c (bara)	1.05	± 0.95
T_{01} (K)	287.00	± 0.35
p_{01} (bara)	5.00	± 0.20
T_{0h}'(K)	303.00	± 0.33

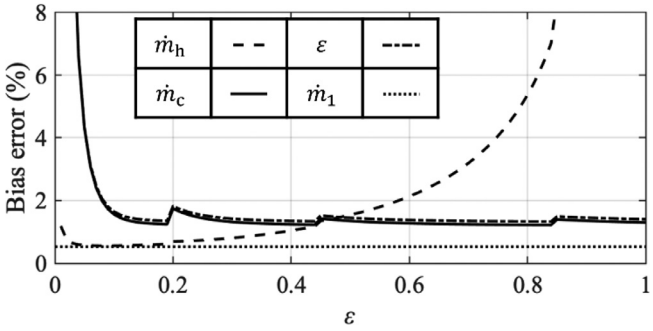

Fig. 23. Estimated percentage bias errors for mass flow rates and ε as a function of ε.

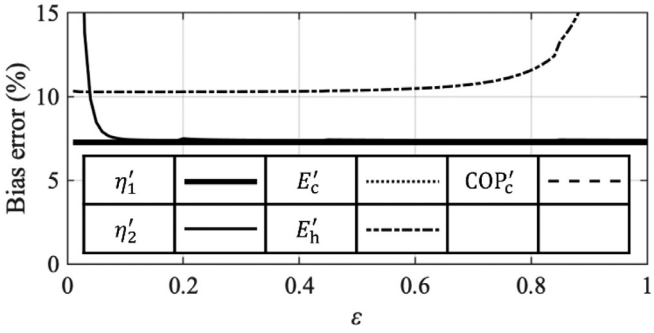

Fig. 24. Estimated percentage bias errors for performance parameters as a function of ε for $p_{01}/p_c = 5.0$.

Percentage bias errors for performance metrics are presented in Fig. 24. Looking first at η_1' (average value of 0.16 for data considered), the percentage bias error is constant with value 7.0%: this is because ε does not appear in the definition (Eq. (9)). For η_2', E_c' and COP_c' (average values of 0.074, 0.026 and 0.059, respectively, for the data considered) the percentage bias errors have similar trends because the uncertainties in these parameters are dominated by uncertainties in ε, T_{01} and T_{0c}' and these terms appear in a similar form in the equations for RSS error propagation for these three parameters. They have approximately constant values of 7.4% in the range $0.10 < \varepsilon \leq 1.0$, and rapidly explode for $\varepsilon \leq 0.10$. The rapid increase for low values of cold-gas mass fraction is due to rapid increase in uncertainty in ε in this range (see Fig. 23) Finally, E_h' (average value of 0.023 for the data considered) has percentage bias error of approximately 10% in the range $0.0 < \varepsilon \leq 0.60$ before rising monotonically in the range $0.60 < \varepsilon \leq 1.0$. The error in E_h' is higher than that in E_c' because it is driven by uncertainty in T_{0h}', which has higher percentage bias error than T_{0c}' (see Table 3).

Appendix 2. Details of transient correction implementation

The procedure used to determine the apportionment of the transient heat flux correction between the hot and cold streams is now discussed. A minimisation technique was used, in which $k_1(\varepsilon)$ was determined (see Eqs. (18) and (19)) such that the change in corrected hot and cold-exit temperature separations over the duration of a run is minimised.

It is assumed that the transient heat flux correction primarily affects the hot-exit flow over most of the range of ε, due to more intimate contact between this stream and the wall. There are

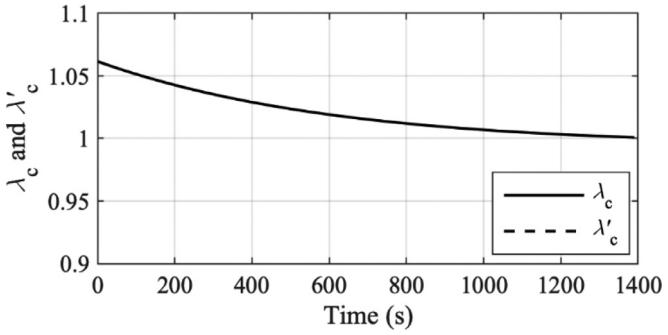

Fig. 25. Normalised cold-exit temperature separation before (λ_c) and after (λ'_c) transient heat flux correction for a typical run ($p_{01}/p_c = 3.0$; $\varepsilon = 0.69$, and $\alpha = 0.78$).

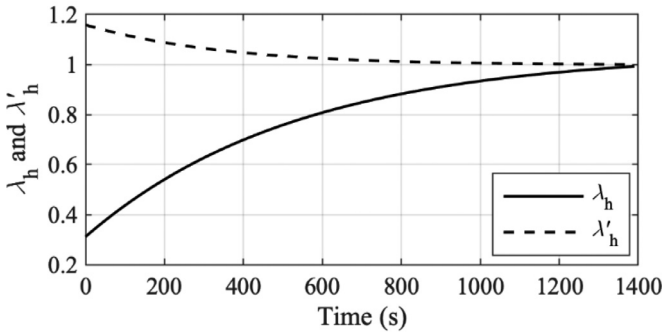

Fig. 26. Normalised hot-exit temperature separation before (λ_h) and after (λ'_h) transient heat flux correction for a typical run ($p_{01}/p_c = 3.0$; $\varepsilon = 0.69$, and $\alpha = 0.78$).

two physical constraints on $k_1(\varepsilon)$, however: $k_1(\varepsilon) = 0$ at $\varepsilon = 0$ (no cold-gas outlet flow); and $k_1(\varepsilon) = 1$ at $\varepsilon = 1$ (no hot-gas flow).

A linear hinge function of the following form is used:

$$k_1(\varepsilon, \alpha) = \begin{cases} 0, & \varepsilon < \alpha \\ \left(\frac{\varepsilon-\alpha}{1-\alpha}\right), & \varepsilon \geq \alpha \end{cases} \tag{20}$$

where α is a constant representing the value of ε at the hinge point. The optimum value of α is determined by a minimisation process, giving the function $k_1(\varepsilon)$. The linear hinge function satisfies both physical limits, and the loose argument—based on CFD observations—that the heat flux correction primarily affects the hot stream over most of the range of ε.

In the optimisation procedure a number of long runs (1400 s) of data were taken (see, for example, Fig. 25 data) at a range of ε, and corrected normalised cold-exit and hot-exit temperature separations defined by

$$\lambda'_c(\alpha, t) = \frac{1 - \theta'_c(\alpha, t)}{1 - \theta'_c(\alpha, t = 1400)} \tag{21}$$

and

$$\lambda'_h(\alpha, t) = \frac{\theta'_h(\alpha, t) - 1}{\theta'_h(\alpha, t = 1400) - 1} \tag{22}$$

Here the temperature separation at time t is normalised by the temperature separation at $t = 1400$ s. Similar *uncorrected* (for heat flux correction) non-dimensional temperature separation parameters λ_c and λ_h can be defined by substituting uncorrected non-dimensional temperatures θ_c and θ_h into Eqs. (21) and (22). Resulting trends λ'_c and λ_c, and corresponding trends λ'_h and λ_h are shown in Fig. 25 and Fig. 26, respectively. These data are (arbitrarily) for a run with $p_{01}/p_c = 3.0$ and $\varepsilon = 0.69$, and are presented for $\alpha = 0.78$ (this is later determined to be the optimum value).

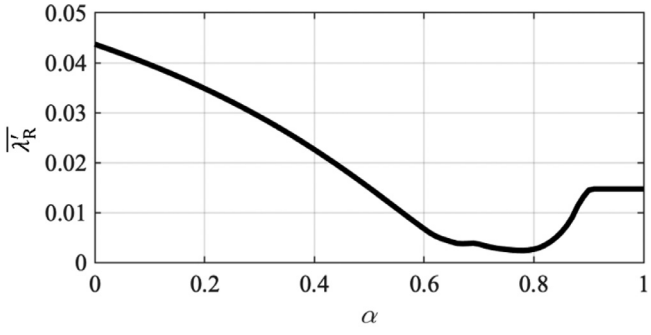

Fig. 27. $\overline{\Delta\lambda'_R}$ as a function of α.

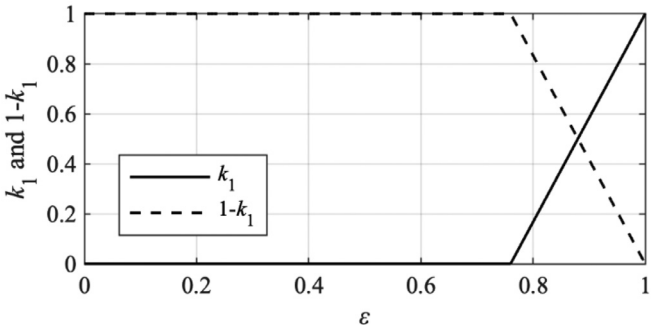

Fig. 28. $k_1(\varepsilon)$ and $1 - k_1(\varepsilon)$ as a function of ε for $\alpha = 0.78$.

Because of the normalisation procedure (i.e. Eqs. (21) and (22)) the characteristics in time of $\lambda'_c, \lambda_c, \lambda'_h$ and λ_h must pass through unity at $t = 1400$ s. As expected, the uncorrected trends λ_c and λ_h are quasi-asymptotic to unity, but with finite gradient at $t = 1400$ s. The quasi-asymptotic trend is due to a reduction in the magnitude of the heat transfer correction with time, and the finite gradient at $t = 1400$ s is due to finite uncorrected heat flux at this condition. Now consider the corrected trends λ'_c and λ'_h. It is first noted that the deviation from unity is everywhere lower than or equal to the corresponding trends λ_c and λ_h, showing that the heat flux correction has increased the stability of the non-dimensional temperature characteristics. It is also noted that the trends are visually true-asymptotic to unity, suggesting that the corrected signals have low residual error at high t. To quantify deviations from unity, the RMS deviations from unity across the entire time series of $\lambda'_c, \lambda_c, \lambda'_h$ and λ_h are taken. These quantities (evaluated over the time period at $0 < t < 1400$ s) are referred to as $\Delta\lambda'_c(\alpha)$, $\Delta\lambda_c$, $\Delta\lambda'_h(\alpha)$ and $\Delta\lambda_h$. Taking the average over a number of runs with different ε, quantities $\overline{\Delta\lambda'_c}(\alpha)$, $\overline{\Delta\lambda_c}$, $\overline{\Delta\lambda'_h}(\alpha)$ and $\overline{\Delta\lambda_h}$ are defined. Overall residuals for the entire data set are also defined by

$$\overline{\Delta\lambda'_R}(\alpha) = \sqrt{\overline{\Delta\lambda'_c}(\alpha)^2 + \overline{\Delta\lambda'_h}(\alpha)^2} \tag{23}$$

and

$$\overline{\Delta\lambda_R} = \sqrt{\overline{\Delta\lambda_c} + \overline{\Delta\lambda_h}} \tag{24}$$

$\overline{\Delta\lambda'_R}$ is plotted in Fig. 27 as a function of α. The minimum value occurs at $\alpha = 0.78$, with corresponding residual value, $\overline{\Delta\lambda'_R}(0.78) = 0.0024$. At the minimum point, $\overline{\Delta\lambda_R}/\overline{\Delta\lambda'_R} = 22.0$, demonstrating that the stability of the non-dimensional characteristics is significantly improved when the transient correction is applied. The final forms of k_1 and $1 - k_1$ as a function of ε Eqs. (18) and (19) are plotted in Fig. 28. The characteristics $k_1(\varepsilon)$ are used in this paper for apportioning the transient correction term between hot and cold streams.

References

[1] G.J. Ranque, Experiments on expansion in a vortex with simultaneous exhaust of hot air and cold air, J. Phys. Radium 4 (1933) 112–114 (Paris).
[2] Y. Raiskii, L. Tunkel, Influence of vortex-tube configuration and length on the process of energetic gas separation, J. Eng. Phys. 27 (6) (1974) 1578–1581.
[3] O. Aydin, M. Baki, An experimental study on the design parameters of a counterflow vortex tube, Energy 31 (14) (2006) 2763–2772.
[4] A.T. Pise, K.D. Devade, Investigation of refrigeration effect using short divergent vortex tube, Int. J. Earth Sci. Eng. 5 (1) (2012) 378–384.
[5] M. Saidi, M. Valipour, Experimental modelling of vortex tube refrigerator, Appl. Therm. Eng. 23 (15) (2003) 1971–1980.
[6] A. Nouri-Borujerdi, M. Bovand, S. Rashidi, K. Dincer, Geometric parameters and response surface methodology on cooling performance of vortex tubes, Int. J. Sustain. Energy 36 (9) (2016) 872–886.
[7] P. Promvonge, S. Eiamsa-ard, Investigation on the vortex thermal separation in a vortex tube refrigerator, ScienceAsia 31 (2005) 215–223.
[8] U. Behera, P.J. P.aul, S. Kasthurirengan, R. Karunanithi, S.N. Ram, K. Dinesh, S. Jacob, CFD analysis and experimental investigations towards optimizing the parameters of Ranque-Hilsch vortex tube, Int. J. Heat Mass Transf. 48 (2005) 1961–1973.
[9] R. Westley, Optimum Design of a Vortex Tube For Achieving Large Temperature Drop Ratios, 30, The College of Aeronautics, Cranfield, 1955 Note.
[10] K.D. Devade, A.T. Pise, Comparative Study of Short Straight Divergent Vortex Tube and Long Convergent Vortex Tube, Pudukottai, 2014.
[11] K.D. Devade, A.T. Pise, Parametric analysis of thermal performance of Ranque-Hilsch vortex tube, J. Therm. Eng. 4 (5) (2018) 2333–2354.
[12] N. Pourmahmoud, H. Zadeh, O. Moutaby, A. Bramo, CFD analysis of helical nozzles effects on the energy separation in a vortex tube, Therm. Sci. 16 (1) (2012) 151–166.
[13] S. Eiamsa-ard, Experimental investigation of energy separation in a counter-flow Ranque–Hilsch vortex tube with multiple inlet snail entries, Int. Commun. Heat Mass Transf. 37 (6) (2010) 637–643.
[14] V. Kirmaci, Exergy analysis and performance of a counter flow Ranque–Hilsch vortex tube having various nozzle numbers at different inlet pressures of oxygen and air, Int. J. Refrig. 32 (7) (2009) 1626–1633.
[15] N. Agrawal, S.S. Naik, Y.P. Gawale, Experimental investigation of vortex tube using natural substances, Int. Commun. Heat Mass Transf. 52 (2014) 51–55.
[16] K. Stephan, S. Lin, M. Durst, F. Huang, D. Seher, An investigation of energy separation in a vortex tube, Int. J. Heat Mass Transf. 26 (3) (1983) 341–348.
[17] BS EN ISO 9300Measurement of Gas Flows By Means of Critical Flow Venturi Nozzles, BS EN ISO 9300, London, United Kingdom, 2005 0 580 46705 8.
[18] BS EN ISO 5167-3Measurement of Fluid By Means of Pressure Differential Devices Inserted in Circular Cross-Section Conduits Running Full - Part 3: Nozzles and Venturi Nozzles, BS EN ISO 5167-3, London, United Kingdom, 2003 0 580 41455 8.
[19] J.R. Roebuck, The Joule-Thomson effect in air, Proc. Am. Acad. Arts Sci. 60 (13) (1925) 537–596.
[20] T.L. Bergman, A.S. Lavine, F.P. Incropera, D.P. Dewitt, Fundamentals of Heat and Mass Transfer, 7th ed., John Wiley & Sons, United States of America, 2011 978-0470-50197-9.